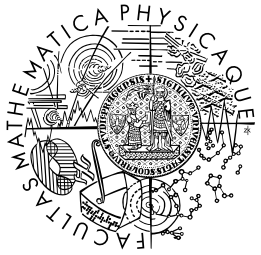

FACULTY
OF MATHEMATICS
AND PHYSICS
Charles University

DOCTORAL THESIS

Dávid Hvizdoš

Modeling the dissociative recombination of light ions

Ústav fyzikální chemie J. Heyrovského AV ČR

Supervisor of the doctoral thesis: Mgr. Roman Čurík, Ph.D.

Study programme: Theoretical Physics, Astronomy and Astrophysics

Study branch: Theoretical Physics, Astronomy and Astrophysics

Prague 2020

I declare that I carried out this doctoral thesis independently, and only with the cited sources, literature and other professional sources. It has not been used to obtain another or the same degree.

I understand that my work relates to the rights and obligations under the Act No. 121/2000 Sb., the Copyright Act, as amended, in particular the fact that the Charles University has the right to conclude a license agreement on the use of this work as a school work pursuant to Section 60 subsection 1 of the Copyright Act.

In ..... date ....

Author's signature

First, I would like to thank my supervisor Mgr. Roman Čurík, Ph.D. for all the help, guidance and expert knowledge he has provided me during my Ph.D. studies.

I would also like to thank prof. Chris H. Greene for all the invaluable advice and insights he has given us throughout this project and also for making possible my scholarly visit to Purdue University which was a truly enriching experience.

Thirdly, I would like to thank Mgr. Michal Tarana, Ph.D. for all the mathematical, programming and physics help and references he has provided me during my stay at the J. Heyrovský Institute of Physical Chemistry.

Finally, I wish to thank doc. RNDr. Karel Houfek, Ph.D. for introducing me to theoretical atomic physics and building the foundation for my doctoral project.

Title: Modeling the dissociative recombination of light ions

Author: Dávid Hvizdoš

Institute: Ústav fyzikální chemie J. Heyrovského AV ČR

Supervisor: Mgr. Roman Čurík, Ph.D., Ústav fyzikální chemie J. Heyrovského AV ČR

Abstract: The purpose of this work and the project under which it was created is to develop, compare and validate several theoretical approaches and computation methods used to calculate the cross sections of dissociative recombination. For the most part it is concerned with the indirect dissociative recombination of molecular ions of H_2^+ in the singlet ungerade channels computed with three distinct approaches. First, the fully numerically solvable two-dimensional approach developed at ÚTF MFF UK as a part of my master's thesis. Second, a vibrational frame transformation method based on the work of Chang and Fano [E. S. Chang and U. Fano, Phys. Rev. A **6**, 173 (1972)] and then enhanced into a full energy-dependent form by Gao and Greene [H. Gao and C. H. Greene, J. Chem. Phys. **91**, 3988 (1989)], [H. Gao and C. H. Greene, Phys. Rev. A **42**, 6946 (1990)], further improved by our own revisions. Third, a two-dimensional R-matrix method based on matching exact 2D solutions from a small interaction region to asymptotic solutions in the non-interacting region. We thoroughly discuss the various advantages and caveats of these methods and, in the later chapters, present our work on employing them for the realistic recombination of $HeH^+ + e^-$. Furthermore, we attempt to extend the presented models to the description of the direct dissociative recombination of $H_2^+ + e^-$ in the singlet gerade symmetry.

Keywords: dissociative recombination, molecular ions, vibrational frame transformation, multichannel quantum defect theory

Contents

Introduction

The process wherein an ionised gas is neutralized by interacting with electrons is called recombination. For atomic ions the only way to bind an electron and get rid of excess energy (barring the presence of some third body) is photon emission which makes recombination a slow and inefficient process for them. For diatomic and larger molecular ions though, the energy can be channelled into breaking chemical bonds and the excess becomes the kinetic energy of the breakup products. This is called dissociative recombination (DR) and it is a highly efficient and thus important pathway to neutralizing ionised gasses [1]. Symbolically, it is

$$\mathrm{AB}^+ + e^- \to \mathrm{A} + \mathrm{B}(n) \ ,$$

where one of the fragments is typically electronically excited.

Indeed, it is considered crucial to the understanding of both molecular plasma dynamics within interstellar clouds and the neutralization of gasses inside the Earth's upper atmosphere. Despite its importance it is a poorly understood process. This is due to the fact that accurate results and descriptions of DR are very challenging from both an experimental and theoretical perspective. This stems mostly from the fact that the Hamiltonian describing the overall interaction always contains a coulombic term for the long range electron-ion interaction. From a theoretical standpoint, this makes asymptotic (in the electronic coordinate) solutions more complicated and their connection to a short-range interaction region needs to be treated carefully. The presence of infinite series of Rydberg states accumulating energetically under each vibrational excitation (VE) threshold results in rich and dense resonance structures in cross section and rate coefficient graphs [1].

This means that for a meaningful experimental study, which hopes to identify these structures, a very high energetic resolution is needed. Experiments have started reaching this level of accuracy only recently [2]. Historically, DR experiments have been much less precise and have often shown only the correct order of magnitude of cross sections or rate coefficients rather than any precise structure. For more information on the history of DR experiments and theoretical description one should read the excellent book by Mats Larsson and Ann E. Orel [1].

Similarly, due to the complexity of the problem, the previous theoretical studies of DR were often based on strongly approximative assumptions to facilitate computation at the expense of accuracy (since comparisons with experiments would only compare the correct order of magnitude and general shape of curves).

And so, with the advent of better experimental equipment, the main goal of our work in the past years is the development of a more accurate theoretical toolkit and its efficient implementation. However, since theoretical methods allow for resolutions even finer than the accurate experiments, we first aim to develop and implement multiple methods to benchmark and compare against each other. For the sake of simplicity we mostly focus on the DR in the system $\mathrm{H}_2^+ + e^-$ with the resulting technique also applied to $\mathrm{HeH}^+ + e^-$ for the eventual experimental comparisons. We thus start by developing and comparing three theoretical approaches to computing the indirect mechanism (more on that in chapter 1) of

$H_2^+ + e^-$ DR on a two-dimensional model:

- A straightforward and numerically exact solution of the model (actually developed as part of my master's thesis [3]), which is rather slow compared to the others but serves as a first benchmark.
- An approximative approach that employs the frame transformation (FT) method first developed by Chang and Fano [4] combined with multichannel quantum defect theory (MQDT - for more information on quantum defects see Seaton's work [5]). We expand the first highly approximative "energy-independent" approach according to the theory laid out by Gao and Greene [6, 7] and further extended by us.
- A two-dimensional R-matrix method that solves the problem exactly in some limited two-dimensional box with significant electron-nuclear coupling and connects these solutions on the box surface to analytical outer region solutions via MQDT. This method can also be adjusted to a Born-Oppenheimer approximation (BOA) form as first proposed by Schneider *et al.* [8] to test the validity of this approximation for DR.

The expanded second approach is then used for the aforementioned experimental comparison of DR of $HeH^+ + e^-$, and afterwards, we create a model describing the direct mechanism (also explained in chapter 1) of $H_2^+ + e^-$ DR and adapt one of the approaches to treat this more complicated case.

In order to differentiate between citations which are not a direct part of this work and our own publications, we will be using the letters [A], [B], [C] and [D] to reference those that resulted from my Ph.D. work. Unless stated otherwise, all of the physical values presented are in atomic units, so common constants are $\hbar = e = m_e = 4\pi\epsilon_0 = 1$. Distances are measured in units of the Bohr radius $r_{Bohr} \doteq 5.291772 \times 10^{-11}$ m, cross sections in bohr^2 and energies in hartrees $E_h \doteq 27.211386$ eV $\doteq 219474.63$ cm^{-1} $\doteq 4.359744 \times 10^{-18}$ J. The final graphs depicting cross-section results often use electronvolts for energy units and vibronic energy comparisons use wave numbers (cm^{-1}). Whenever we type matrices without indices they will be underlined (e.g. $\underline{S}$) to differentiate them from scalar quantities.

On a technical note, the numerical implementation of integrals over the electronic and nuclear coordinates and the description of corresponding wave functions employed a basis of B splines [9]. The technical details (basis size and the grid parameters) can be found inside our published papers [A], [B], [C], [D].

1. Dissociative recombination and molecular hydrogen

In general, we recognize two different pathways along which dissociative recombination can happen. They are called the direct and indirect mechanism of the DR. The direct mechanism is depicted in Fig.1.1a and described thusly: An electron collides with a molecular ion AB^+ getting captured and converting its kinetic energy into electronic excitation and the system becomes AB^{**}. Though unstable, if the curve of AB^{**} is repulsive enough, the molecule will dissociate before it can autoionize.

However, there are cases where no such "AB^{**}" resonance exists (for example with H_2 in the singlet ungerade symmetry). In such instances DR can still occur via the second, indirect mechanism. It is depicted in Fig.1.1b and described thusly: the incoming electron converts its kinetic energy into vibrational excitation of the molecule and gets captured in a Rydberg state which is a part of a series of states accumulating under the AB^+ potential curve. With sufficient incoming electron energy the system can dissociate via low enough Rydberg states.

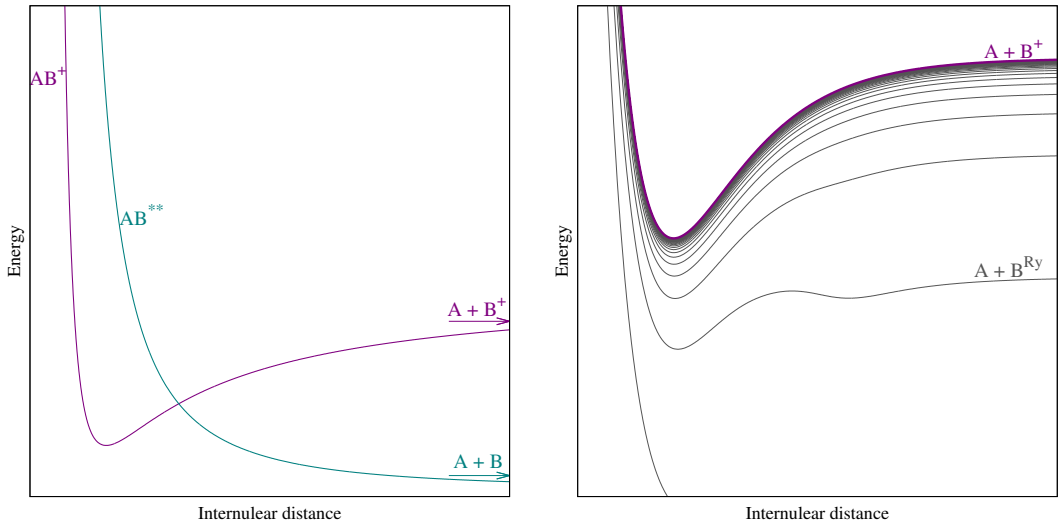

(a) Direct DR (b) Indirect DR

Figure 1.1: A visualization of the types of dissociative recombination.

The series of Rydberg states is always present and causes the creation of infinite series of resonances energetically accumulating under each vibrational excitation threshold. It is apparent that even in the simple case of H_2^+ DR becomes a highly complex problem with many quirks and caveats.

1.1 Model of indirect DR for $H_2^+ + e^-$

Throughout the publications [A], [B], [C] we study the indirect DR on the model of the singlet ungerade symmetry channels of H_2. All the theoretical descriptions, that we employ, start by choosing correct model Hamiltonians to describe the

interaction between the target molecular ion and the incoming electron. Since we have chosen to study simple systems with only one nuclear and one electronic degree of freedom (after separating out the rotational parts), the model potentials are just functions of two coordinates (R for the internuclear separation and r for the electronic distance from the molecule's center). The full Hamiltonian for the indirect dissociative recombination model is thus

$$H(R,r) = H_0(R,r) + V(R,r) = H_\mathrm{n}(R) + H_\mathrm{e}^l(r) + V(R,r)\ , \tag{1.1}$$

with

$$\begin{aligned}
H_\mathrm{n}(R) &= -\frac{1}{2M}\frac{\partial^2}{\partial R^2} + V_0(R)\ , & (1.2)\\
H_\mathrm{e}^l(r) &= -\frac{1}{2}\frac{\partial^2}{\partial r^2} - \frac{1}{r} + \frac{l(l+1)}{2r^2}\ , & (1.3)\\
V_0(R) &= D_0\left(e^{-2\alpha_0(R-R_e)} - 2\,e^{-\alpha_0(R-R_e)}\right)\ , & (1.4)\\
V(R,r) &= -\alpha_1\left(1-\tanh\frac{\alpha_2 - R - \alpha_3 R^4}{7}\right)\tanh^4\left(\frac{R}{\alpha_4}\right)\frac{e^{-r^2/3}}{r}\ , & (1.5)
\end{aligned}$$

where $M = 918.076$ a.u. denotes the reduced mass of H_2^+, l is the angular momentum of the incoming electron[1] and the potential parameters are $\alpha_1 = 1.6435$, $\alpha_2 = 6.2$, $\alpha_3 = 0.0125$, $\alpha_4 = 1.15$, $D_0 = 0.1027$ hartree, $\alpha_0 = 0.69$ bohr^{-1} and $R_e = 2.0$ bohr. The Morse potential $V_0(R)$ models the ground-state potential curve of the target cation. The model potential $V(R,r)$ describing the interaction between the electron and the molecule was taken from E.L. Hamilton's thesis [10]. It is tailored to reproduce the exact e^-+H_2^+ coupling potential with high accuracy. Something to note about this model interaction is that though it reproduces the adiabatic potential curves of the $^1\Sigma_u^+$ states of H_2 quite closely, the lowest state potential curve coming from this model is actually quite unphysical. Fortunately, it is energetically well below all the other curves (by cca. 37 eV) and ends up not having any noticeable impact on the results of our studies (e.g. the connected cross sections are many orders of magnitude below any physical ones). This holds true for every single one of the approaches that we have used the model interaction in. For more details on the potential itself refer to Hamilton's thesis [10]. The potentials have the following asymptotic limits

$$\begin{aligned}
V(R,r) &= 0\ , \qquad \text{for} \quad r \geq r_0\ , & (1.6)\\
V(R,r) &= V(R_0,r)\ , \quad \text{for} \quad R \geq R_0\ , & (1.7)\\
V_0(R) &= 0\ , \qquad \text{for} \quad R \geq R_0\ , & (1.8)
\end{aligned}$$

for some reasonably small r_0 and R_0. This naturally leads to a partitioning of the configuration space (as shown in Fig. 1.2) into an inner (reaction zone) and outer regions in such a way that nuclear and electronic Hamiltonians are completely separable in the outer region. The studied outgoing channels in this model are vibrational excitation and dissociative recombination. The upper right part of Fig. 1.2 contains an additional "path to dissociative scattering" (no recombination) but that is a process quite outside our studied range of energies and thus not relevant in this work. The model for the direct DR of $H_2^+ + e^-$ will be described in chapter 6.

[1] In the indirect case we only consider the incoming electronic p-wave so $l = 1$. For this reason the chapters treating the indirect DR of H_2^+ omit writing the l and we just write $H_\mathrm{e}(r)$.

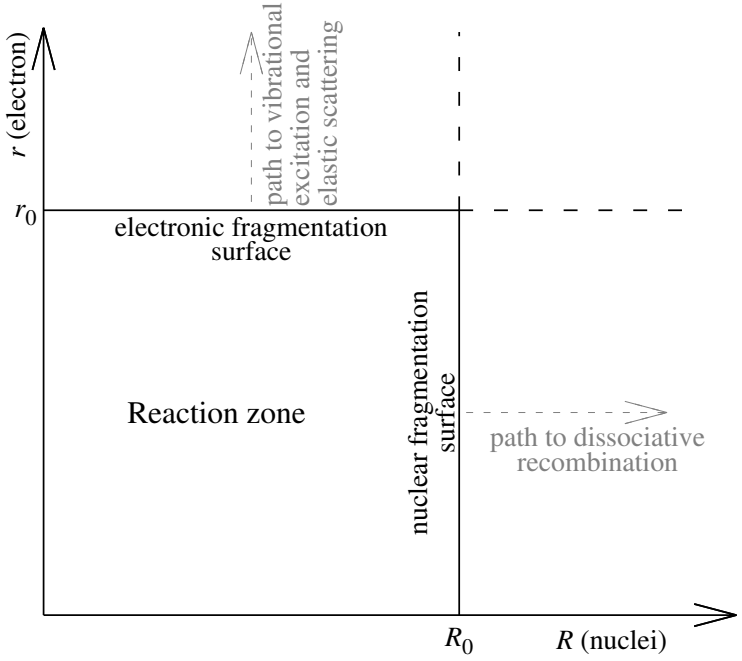

Figure 1.2: Configuration space partitioning.

1.2 First two-dimensional method

Upon constructing the full Hamiltonian (1.1) we can write the Schrödinger equation

$$(E - H(R, r))\psi_E(R, r) = 0 \, . \tag{1.9}$$

The method of solving this equation described in my master's thesis [3] is our first attempt at computing the indirect DR of the $H_2^+ + e^-$ model. It was done by solving (1.9) in a large 2D space without any further approximations. It is based on the 2D numerical approach of Houfek, Rescigno and McCurdy [11], originally used to get cross sections of vibrational excitation and dissociative electron attachment. The method uses exterior complex scaling (ECS)[2] in both the electronic and the nuclear coordinate to achieve seamless boundary condition implementation for incoming and outgoing waves. The continuous variables are represented using the finite element method (FEM) with discrete variable representation (DVR). Because of this we call it the 2D FEM-DVR-ECS method.

A straightforward solution of the Schrödinger equation (1.9) with the aim of computing both the VE and the DR cross sections requires a description of not only the wave functions connected to the open and weakly closed outgoing channels, but also all of the intermediate electronic Rydberg states to obtain the corresponding closed-channel resonances. Since there is an infinite number of these accumulating under each VE threshold and the higher states reach increasingly farther in the electronic coordinate, a complete numerical description

[2]We will also use exterior complex scaling in the nuclear coordinate in chapter 4 to obtain our nuclear vibrational basis. There, we will delve deeper into the exact nature of this coordinate bending.

within a finite space is impossible with this straightforward method. This means that when using a finite grid to represent the 2D space, the cross sections will always have energy windows under each vibrational threshold, where the method is unconverged and will fail to describe all the resonances numerically. These windows of inaccuracy can be theoretically shrunk down to any desired size but at increasingly high computational cost. The implementation used by us had an electronic grid length of 100000 bohrs and the inaccuracy windows were still rather visible (you can see this in the cross-section comparison images in chapter 2). Since we made no further approximations, we consider the results given by this method to be exact outside of the aforementioned inaccuracy windows and they will be used as our first benchmark for later methods.

A more thorough description of the 2D FEM-DVR-ECS approach with all the necessary mathematical rigour can be found in my master's thesis [3] and (slightly less thorough) in our first publication [A]. The approach is unfeasible for more complicated real systems and may take several days of computation (if we desire to really shrink the unconverged result windows) for the same amount of data that an approximative method (like those in chapters 2 and 4) would produce in minutes. A very symbolic comparison of the computation ranges used in our approaches to the DR can be found in Fig. 1.3. It shows at first glance, how the faster methods (used in the later chapters) need only to work in the reaction zone while the 2D FEM-DVR-ECS method operates on a much larger area.

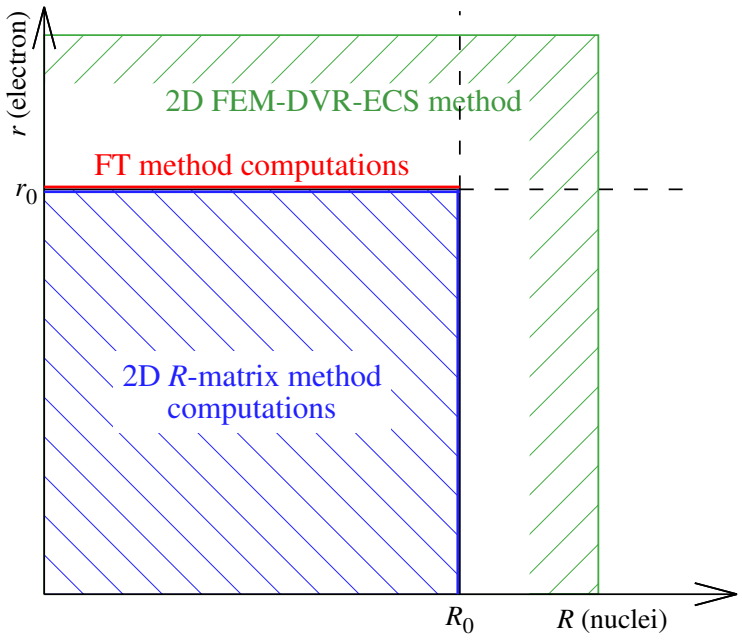

Figure 1.3: A symbolic representation of the computation box sizes and ranges of the three different approaches to computing DR.

2. DR by frame transformation

Historically, one of the most common and successful methods of computing the low-energy cross sections for the VE and the DR processes has been the frame transformation method [4]. In practice the FT is an approach that can be implemented in a computationally highly efficient manner. As opposed to the vibrational excitation via FT, which can be done rather straightforwardly, application of the frame transformation theory in the DR process requires several additional non-trivial approximations and assumptions. Although the FT procedure has been successfully used numerous times in the past (for example DR of H_2^+ [12], H_3^+ [13], LiH^+ [14, 15], NO_2^+ [16], $LiHe^+$ [17], LiH_2^+ [18] and HeH^+ [19, 20]), the employed approximations and assumptions were never tested rigorously. Thus the aim of our first [A] and third [C] studies was to more thoroughly test the method's approximations in a more strict numerical environment. In both cases we have chosen DR of singlet ungerade $H_2^+ + e^-$.

The typical approximations and assumptions in the FT in the DR process are as follows:

- FT methods use the **Born-Oppenheimer** quantum defects to compute the short-range scattering matrix so one must always keep in mind the limitations of the Born-Oppenheimer approximation. It is important to note here that the FT methods only assume the Born-Oppenheimer approximation to hold inside some limited box of the electronic $r \leq r_0$ coordinate.

- As opposed to the vibrational excitation, which is computed directly, the DR cross sections are obtained by computing a subunitary scattering matrix with indices corresponding to the open VE channels. Subunitarity means that the sum of probabilities corresponding to these channels is less than one. The main step that follows is to identify the missing probability flux with the only other open pathway for the system which is the DR [12]. This could be called a **"physical reasoning" assumption**.

- The subunitary scattering matrix is obtained by applying the FT procedure with a basis set of bound and outgoing vibrational wave functions. Historically, a quite successful choice were the so-called Siegert pseudo-states [21, 22] which hold a special orthogonality relation and boundary condition. This results in a rather **unintuitive form of frame-transformed matrices** which was at first guessed and even called *ad hoc* in previous studies [19].

2.1 Energy-independent FT theory in the DR model

In addition to the aforementioned typical FT assumptions, the previous works [12] - [20] made several additional approximations to make the implementation of the FT method simpler. The resulting procedure is called the **energy-independent frame transformation** and our first study [A] follows this approach. The full derivation of the energy-independent FT procedure follows.

We start with the 2D Hamiltonian (1.1),(1.2),(1.3) with $l = 1$, using potentials $V(R, r)$ (1.5) and $V_0(R)$ (1.4). Our goal is to solve the 2D Schrödinger equation

$$\left[H_{\rm e}^{l=1}(r) + H_{\rm n}(R) + V(R, r) - E\right] \psi(R, r) = 0 \ . \tag{2.1}$$

We assume that inside some electronic sphere $r \leq r_0$ BOA holds and the internuclear distance R is a good quantum number within, while for $r > r_0$ the electron-ion interaction is purely Coulomb (thanks to (1.6)). Here the Eq. (2.1) becomes separable in the nuclear and electronic coordinates. Let us denote $f_{j'}(r)$, $g_{j'}(r)$ the regular and irregular Coulomb wave functions for rotational $l = 1$ evaluated at the body-frame momentum $k_{j'} = \sqrt{2\epsilon_{j'}} = \sqrt{2(E - E_{j'})}$ where $E_{j'}$ will be the energy allocated to the nuclear part of the wave function[3]. The pair $\{f, g\}$ is equal to $\{s, -c\}$ from Seaton's work [5, 23]. Let us also denote

$$f_{j'}^{\mp}(r) \equiv \frac{1}{\sqrt{2}}(-g_{j'}(r) \mp i f_{j'}(r)) \ , \tag{2.2}$$

with $i = \sqrt{-1}$. These are the incoming-wave f^- and outgoing-wave f^+ Coulomb functions. Assuming we have a complete vibrational basis $\phi_j(R)$ satisfying

$$H_{\rm n}(R)\phi_{j'}(R) = E_{j'}\phi_{j'}(R) \ , \tag{2.3}$$

we can write the j'-th independent BOA solution of the Schrödinger equation (2.1) in the inner region $r \leq r_0$ at the boundary $r = r_0$ as

$$\psi_{j'}(R, r_0) = \phi_{j'}(R) N(R, \epsilon_{j'}) \left[f_{j'}^-(r_0) - f_{j'}^+(r_0) e^{2\pi i \mu(\epsilon_{j'}, R)}\right] \ , \tag{2.4}$$

where $\mu(\epsilon_{j'}, R)$ is the body-frame quantum defect and $N(R, \epsilon_{j'})$ is a normalization factor. The normalization factor can be omitted for reasons that we will explain further down in this chapter. In the outer region $r > r_0$ the solution of (2.1) is a general linear combination of $\phi_n(R) f_n^-(r)$ and $\phi_n(R) f_n^+(r)$ due to the separability of the Hamiltonian. A matching of the inner- and outer-region solutions at the boundary gives

$$\phi_{j'}(R) \left[f_{j'}^-(r_0) - f_{j'}^+(r_0) e^{2\pi i \mu(\epsilon_{j'}, R)}\right] = \sum_n \phi_n(R) \left[f_n^-(r_0) A_{nj'} - f_n^+(r_0) B_{nj'}\right] \ . \tag{2.5}$$

A knowledge of the orthogonality relations of ϕ_j leads to the construction of a linear one-index functional $F_j[\ .\ ]$ which acts on the space of R-dependent functions satisfying

$$F_j[\phi_{j'}] = \delta_{jj'} \ , \text{ for all } j, j' \ . \tag{2.6}$$

This functional is crucial for extracting the scattering matrix from (2.5). Following suit of previous studies, we used the basis $\phi_{j'}(R)$ of Siegert pseudo-states on the interval $0 \leq R \leq R_0$. They satisfy the Eq. (2.3) with the following boundary conditions

$$\begin{aligned} \phi_{j'}(0) &= 0 \ , \\ \left(\frac{\mathrm{d}}{\mathrm{d}R} - iK_{j'}\right) \phi_{j'}(R)\Big|_{R=R_0} &= 0 \ , \end{aligned} \tag{2.7}$$

[3]Note that this notation is according to the latter publications [B], [C], [D] and that our first publication [A] actually had the symbols ϵ_j and E_j swapped.

where $K_{j'} = \sqrt{2E_{j'}}$ is in general a complex quantity (it is purely imaginary for the bound and anti-bound states). The non-trivial Siegert pseudo-state orthogonality relations

$$\int_0^{R_0} \phi_j(R)\phi_{j'}(R)\mathrm{d}R + i\frac{\phi_j(R_0)\phi_{j'}(R_0)}{K_j + K_{j'}} = \delta_{jj'} \ , \tag{2.8}$$

lead to the following form of $F_j[\ .\ ]$:

$$F_j[h(R)] = \int_0^{R_0} \mathrm{d}R\phi_j(R)h(R) + i\phi_j(R_0)\left[\left(K_j - i\frac{\mathrm{d}}{\mathrm{d}R}\right)^{-1} h(R)\right]_{R=R_0} \ , \tag{2.9}$$

where $h(R)$ is now any smooth function of R. For more information about this functional see the appendix in the publication [A] and more details on the Siegert pseudo-states follow in section 2.3. By applying the functional (2.9) to both sides of (2.5) we get

$$f^-_{j'}(r_0)\delta_{jj'} - f^+_{j'}S_{jj'} = f^-_j(r_0)A_{jj'} - f^+_j(r_0)B_{jj'} \ , \tag{2.10}$$

where

$$\begin{aligned} S_{jj'} = &\int_0^{R_0} \mathrm{d}R\phi_j(R)e^{2\pi i\mu(\epsilon_{j'},R)}\phi_{j'}(R) \\ &+ i\phi_j(R_0)\left[\left(K_j - i\frac{\mathrm{d}}{\mathrm{d}R}\right)^{-1} e^{2\pi i\mu(\epsilon_{j'},R)}\phi_{j'}(R)\right]_{R=R_0} \ . \end{aligned} \tag{2.11}$$

The coefficient matrices $\underline{A}, \underline{B}$ are then obtained by applying the Wronskian technique to (2.10). Let us denote $[.,.]$ the Wronskian of two functions of r and let us also assume in the next step that $f^\pm$ are energy independent at r_0, so $f^\pm_j = f^{\pm 4}_{j'}$. We can then write

$$\begin{aligned} B_{jj'} &= \frac{-1}{[f^+_j, f^-_j]}\left([f^-_{j'}, f^-_j]\delta_{jj'} - [f^+_{j'}, f^-_j]S_{jj'}\right) \\ &\xrightarrow{\text{energy-independent} \quad f^+, f^-} S_{jj'} \ , \\ A_{jj'} &= \frac{1}{[f^-_j, f^+_j]}\left([f^-_{j'}, f^+_j]\delta_{jj'} - [f^+_{j'}, f^+_j]S_{jj'}\right) \\ &\xrightarrow{\text{energy-independent} \quad f^+, f^-} \delta_{jj'} \ . \end{aligned} \tag{2.12}$$

Therefore, for the outer-region ($r > r_0$) solution we get

$$\psi_{j'}(R, r) = \sum_j \phi_j(R)\left[f^-_j(r_0)\delta_{jj'} - f^+_j(r_0)S_{jj'}\right] \ . \tag{2.13}$$

Because of the assumption (1.7), the quantum defect is R-independent for $R \geq R_0$ and (2.11) reduces to

$$S_{jj'} = \int_0^{R_0} \mathrm{d}R\phi_j(R)e^{2\pi i\mu(\epsilon_{j'},R)}\phi_{j'}(R) + i\frac{\phi_j(R_0)e^{2\pi i\mu(\epsilon_{j'},R_0)}\phi_{j'}(R_0)}{K_j + K_{j'}} \ . \tag{2.14}$$

This is actually the *ad hoc* form of the frame-transformed S matrix mentioned at the start of the chapter. It was previously successfully used even without

[4] This approximation is reasonable for a small r_0.

a rigorous mathematical derivation but we have found that it is indeed a valid simplification of the more general form (2.11) and it is correct for any frame transformation method using Siegert pseudo-states as long as the nuclear potential $V_0(R)$ is sufficiently negligible at R_0 and the quantum defect $\mu(\epsilon_{j'}, R)$ is flat for $R \geq R_0$ (for more mathematical rigor see the appendix to the publication [A]). In this first study, we further simplified the form (2.14) by assuming that $\mu(\epsilon_{j'}, R)$ is also energy-independent at all values of R.

As is, the form (2.13) still contains both open and closed channels and thus the S matrix within cannot be called a true physical scattering matrix. It is sometimes called a short-range or body-frame scattering matrix. To get to the physical scattering matrix we need to employ the MQDT elimination of closed channels [5, 24]. The objective of this technique is finding such a linear combination of solutions $\psi_{j'}(R, r)$ where the exponentially growing parts of the closed-channel components cancel out. This results in the physical scattering matrix $\underline{S}^{\text{phys}}$ defined for only the open channels. After separating the short-range S matrix into submatrices

$$\underline{S} = \begin{pmatrix} \underline{S}_{oo} & \underline{S}_{oc} \\ \underline{S}_{co} & \underline{S}_{cc} \end{pmatrix} , \tag{2.15}$$

according to which channels are open and closed at the given energy, the physical scattering matrix satisfies

$$\underline{S}^{\text{phys}}(E) = \underline{S}_{oo} - \underline{S}_{oc} \left[\underline{S}_{cc} - e^{-2i\underline{\beta}(E)} \right]^{-1} \underline{S}_{co} , \tag{2.16}$$

where $\underline{\beta}(E)$ is the matrix of effective Rydberg quantum numbers with respect to the closed-channel thresholds E_j

$$\beta(E)_{jj'} = \frac{\pi \delta_{jj'}}{\sqrt{2(E_j - E)}} , \text{ for the closed-channel } j, j' \text{ only.} \tag{2.17}$$

Finally, as per the second point at the start of the chapter, the DR cross section $\sigma^{\text{DR}}_{j'}(E)$ is obtained from the missing probability flux of the subunitary $\underline{S}^{\text{phys}}(E)$

$$\sigma^{\text{DR}}_{j'}(E) = \frac{\pi}{2(E - E_{j'})} \left[1 - \sum_j S^{\text{phys}}_{jj'}(E) S^{\text{phys}\dagger}_{j'j}(E) \right] . \tag{2.18}$$

It is important to note that this cross section is to be interpreted as a sum over all the possible outgoing Rydberg channels for a given total energy E and for the initial vibrational state j'. Naturally, inelastic VE cross sections into individual channels can also be computed as

$$\sigma^{\text{VE}}_{j \leftarrow j'}(E) = \frac{\pi}{2(E - E_{j'})} \left| S^{\text{phys}}_{jj'}(E) \right|^2 , \quad \text{for} j \neq j' . \tag{2.19}$$

A reader well versed in FT methods might also remember that a previous FT paper [13] stresses that the conjugated matrix $S^{\text{phys}\dagger}_{j'j}(E)$ is to be computed separately via a relation analogous to (2.16) with everything apart from the $\underline{\beta}$ matrix complex-conjugated. In our implementation such an approach resulted in slightly worse accuracy than simply complex conjugating the entire $S^{\text{phys}}_{jj'}(E)$ matrix.

2.2 Method summary and results

As mentioned earlier, the described FT method is called the energy-independent frame transformation. What this means is that though the MQDT elimination of closed channels and computation of cross sections still contain explicit energy dependence, several "softly" energy-dependent quantities were considered constant. To summarize and reiterate:

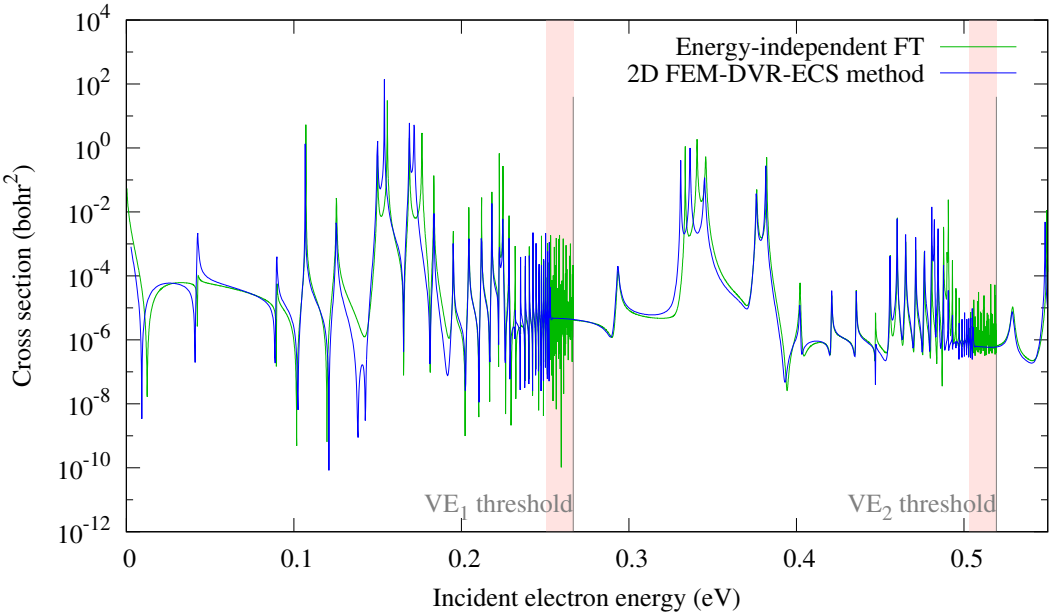

Figure 2.1: Comparison of the DR cross sections. The green line was obtained with the energy-independent FT method and the blue line is the exact numerical 2D FEM-DVR-ECS result. The pink bands show energy windows just below vibrational thresholds where the 2D FEM-DEV-ECS method results are not converged (as described in section 1.2). The collision energies shown are around the first and second vibrational threshold.

- The asymptotic Coulomb functions $f_j^{\pm}(r)$ were chosen such that the Born-Oppenheimer quantum defect $\mu(\epsilon_{j'}, R)$ had a rather small (but non-zero) energy dependence at r_0. In the study we considered the dependence to be exactly zero in our range of energies (further simplifying (2.14)).

- The Coulomb functions themselves are energy-independent in the $r \to 0$ limit. Our frame transformation is computed at the boundary of some small non-zero electronic box but we already considered the Coulomb functions to be energy-independent here. This led to the vanishing Wronskians in (2.12).

- The normalization term $N(R, \epsilon_{j'})$ formally behaves in such a way that it explodes into infinity in the limit of energy-independent quantum defect and asymptotic functions. For a complete nuclear vibrational basis it has been shown by Gao and Greene [6] that the aforementioned energy independence actually results in the omission of $N(R, \epsilon_{j'})$ from (2.4). This omission resulted in a significant simplification of the overall implementation.

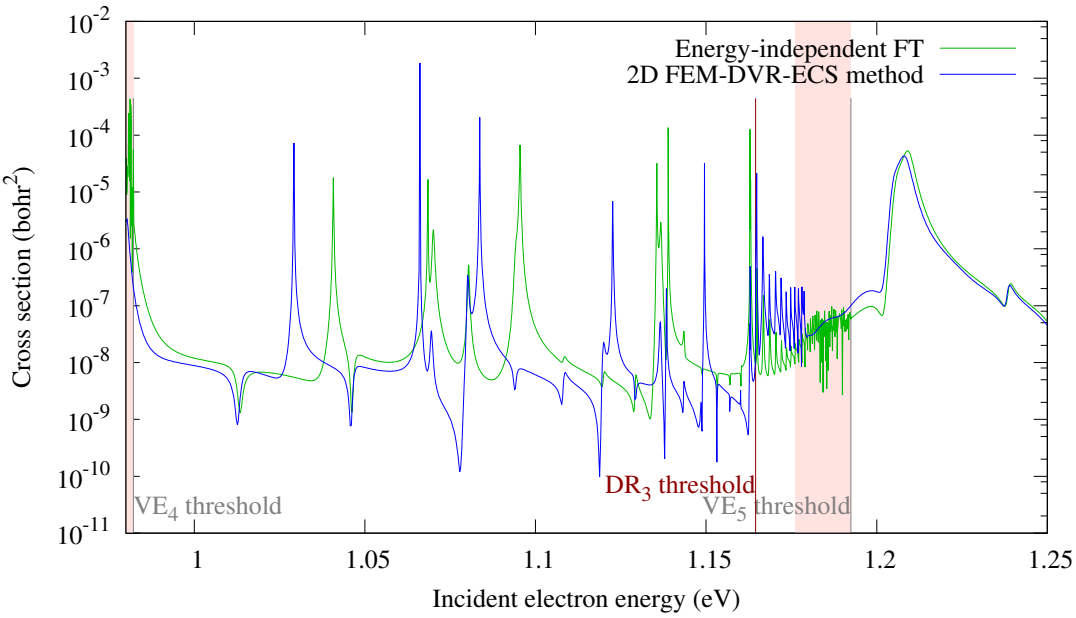

Figure 2.2: Comparison of the DR cross sections. Same colors as in Fig. 2.1 but the energy window is chosen around the third DR channel opening.

Of the "three main assumptions" of our computational procedure, listed at the start of this chapter, the last one was put on firmer grounds by purely analytical means. The "physical reasoning" assumption about missing probability flux cannot be proven analytically, therefore we attempt to justify this step with numerical evidence. The numerical tests comparing the FT method to our benchmarking model were done in a window of 0 to 2 eV collision energies. The results mostly behaved as shown in Fig. 2.1 but around the DR channel openings the

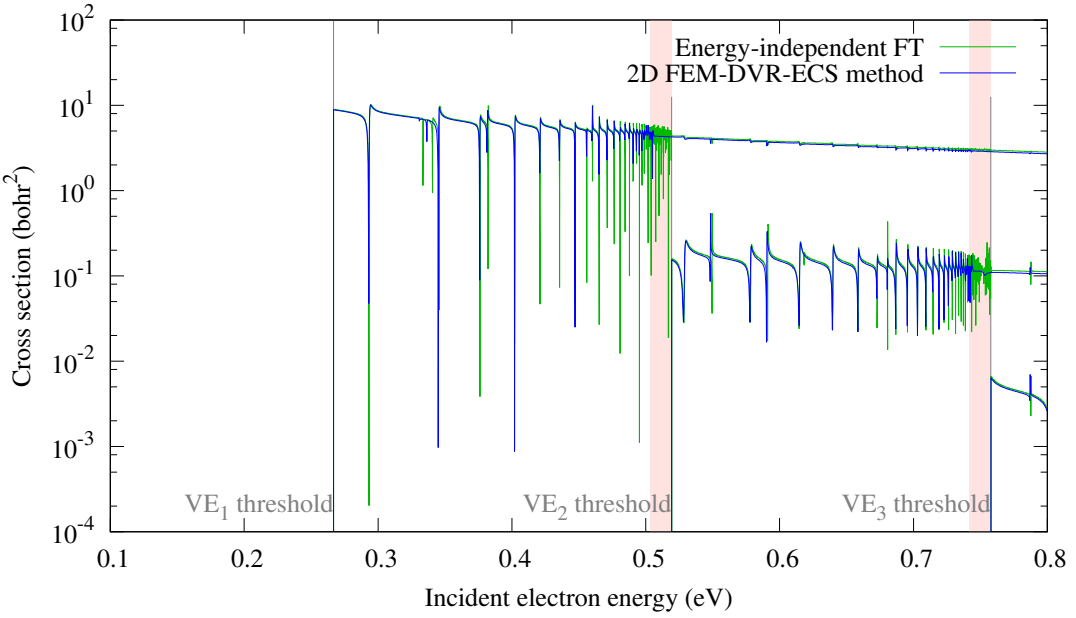

Figure 2.3: Comparison of the VE cross sections with multiple distinguished output channels. Same colors as in Fig. 2.1 with a slightly wider energy window.

accuracy becomes worse as shown in Fig. 2.2 (for more comparisons see the publication [A]).

The numerical tests clearly show that the accuracy of the energy-independent FT method is much better than just an order of magnitude. We observed that the technique of the missing electronic flux (2.18) employed in this work requires reasonably accurate VE transition matrix elements in the physical S matrix. The expression (2.18) leads to a loss of digits when the missing flux (the DR probability) is too low when compared to one. A comparison of VE cross sections is in Fig. 2.3. The coordinate box sizes for our first study were $r_0 = 7$ bohr and $R_0 = 15$ bohr.

2.3 Sources of error

To identify the possible sources of discrepancies we look to the remaining assumptions that we have made (the **energy-independent frame transformation** and the **Born-Oppenheimer approximation**) as well as our choice of a Siegert pseudo-state basis.

Firstly, a very clear indicator of the necessity of a full energy-dependent FT is the last computational test at the end of our first publication where we show how the calculated cross sections change significantly even if we artificially increase the (so far energy-independent) quantum defect value by as little as 2% (Fig. 11 and 12 in Ref. [A]). This is also displayed in Fig. 2.4. The reason for this test is that the positions and shapes of closed-channel resonances are mostly determined by quantum defects at negative energies and Fig. 2.5 shows how the defect increases slightly at these energies and thus the 2% increase test actually leads to better agreement of the lineshapes.

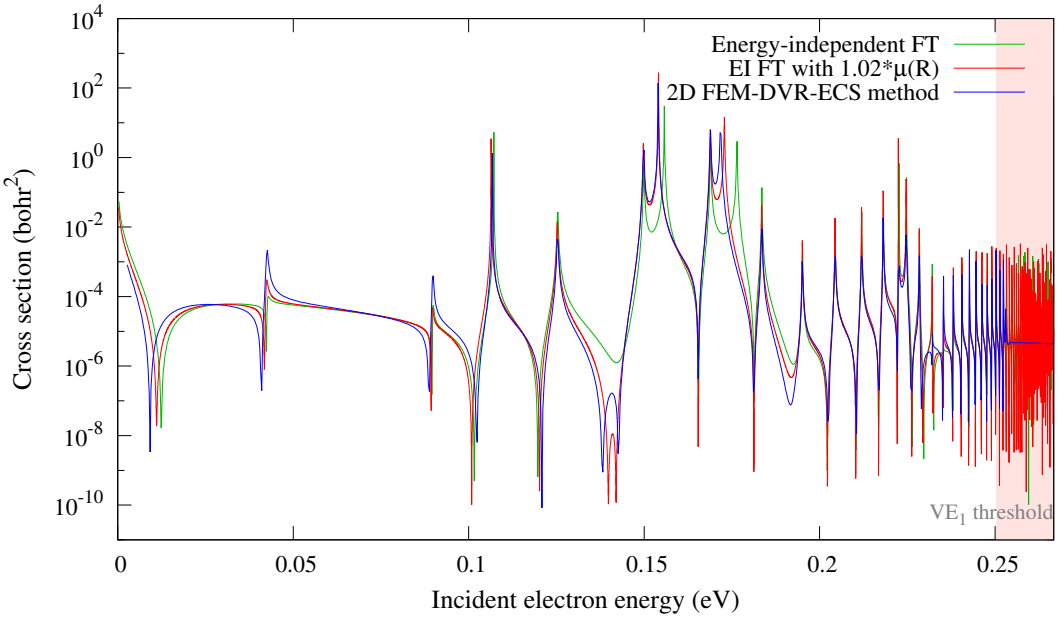

Figure 2.4: Comparison of the DR cross sections for the quantum defect test. We use the same colors as in Fig. 2.1 with the added red curve for the artificially increased quantum defect computation.

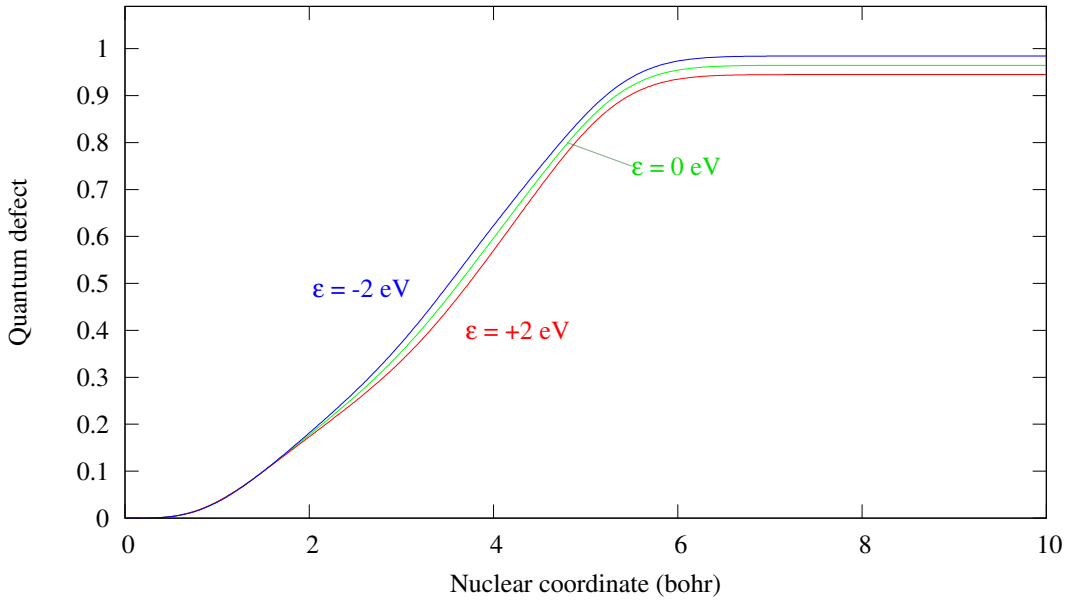

Figure 2.5: The quantum defect $\mu(\epsilon, R)$ of the ungerade model potential evaluated at three energies $\epsilon = -2$ eV, 0 eV, $+2$ eV.

Secondly, Siegert pseudo-states, though successfully and widely used[12, 13], come with their own set of problems when one tries to use them as a basis for scattering problems. Apart from the peculiar orthogonality relations (2.8) there is also the matter of their completeness. Most commonly, in similar numerical studies one would first create a complete basis set of vibrational states by diagonalizing the nuclear Hamiltonian with a chosen boundary condition. Then, one would work with a large enough subset that is sufficiently complete on the relevant part of the Hilbert space. In the case of Siegert pseudo-states, they form a doubly complete basis (i.e. they "cover" the entire Hilbert space exactly twice) due to the nature of their boundary conditions. The entire Siegert pseudo-state basis consists of bound and anti-bound states (assuming the Schrödinger equation at hand has bound state solutions) and outgoing- and incoming-wave continuum states. The two continuum state branches' energies and momenta mirror each other exactly when plotted in the complex plane while the bound and anti-bound states' corresponding energies mostly overlap and momenta lie on the opposite halves of the imaginary axis (shown in Fig. 2.6). To compute the DR we need to use a basis of bound states and outgoing waves. If we simply divide the Siegert pseudo-state basis into two parts, one containing the bound states together with the outgoing-wave states and the other containing the rest (anti-bound and incoming-wave states), we get two basis sets which are almost exactly complete. Unfortunately, such splitting, while physically motivated, is not mathematically exact and leads to small completeness deficiencies within parts of the Hilbert space that are relevant to us. For example, some of the discrepancies visible in Fig. 2.2 were caused by this completeness error (e.g. the energy window from 1.14 eV to 1.16 eV is strongly affected by our chosen Siegert subset's slight over-completeness).

Finally, whether or not our use of BOA in the FT approach was valid was tested in a more indirect way and is the focus of the next chapter 3. The following

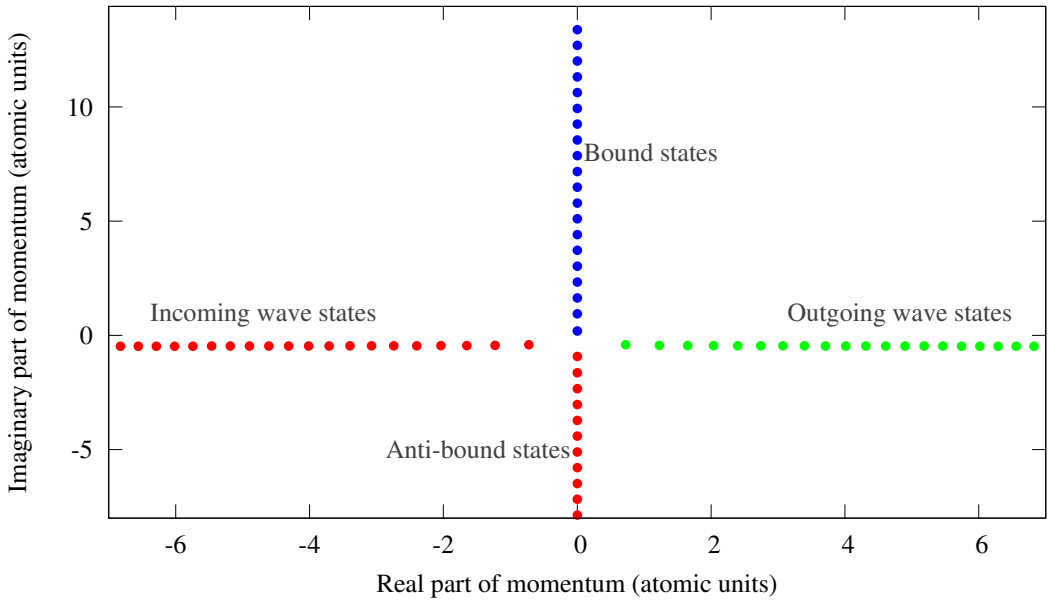

Figure 2.6: Siegert pseudo-state complex momenta example. The less relevant incoming wave and anti-bound states are depicted with red points while bound states are blue and outgoing wave states are green.

process of improving our FT approach is described in chapter 4.

2.4 Computation range clarification

The reader might notice that the explicit form of the coupling potential $V(R, r)$ makes no appearance throughout the Eqs. (2.2-2.18) and could question how exactly the potential enters into the roundabout way of matching the inner and outer solutions and if any effect of said potential is missing. The information is in fact fully there and it is in the form of the BOA body-frame quantum defect, which had been obtained by solving fixed-nuclei versions of the 2D Hamiltonian (1.1) along the electronic coordinate in a $0 < r < r_0$ box. This also means that the Fig. 1.3 can be slightly misleading regarding the computation range of FT. The frame transformation itself only happens on the boundary $r = r_0$ but we need to have BOA information from the entire box beforehand (in the form of $\mu(\epsilon_{j'}, R)$).

3. Two-dimensional R-matrix approach

In our second DR study [B] we aimed for a closer look at the validity of the BOA in those methods that involve the vibrational frame transformation. The processes studied will be the VE and the DR, while the testing model remains as the singlet ungerade channels of the e^-+H_2^+ system. The approximation is a crucial part of all *ab initio* approaches describing elastic and inelastic collisions of electrons with molecules and molecular cations including all the different frame transformation methods that we based our first and third studies on. To test this we have chosen a rather different approach which solves the Schrödinger equation inside a box restricted by r_0 and R_0 and which matches to physically motivated solutions on both the electronic and nuclear surfaces. Thus, it distinguishes between separate DR channels as opposed to our missing flux approach used in the FT method. The starting point of this approach can be traced to Edward Hamilton's thesis [10], where he developed the two-dimensional R-matrix method to model the photo-dissociation and photo-ionization processes. We merely adapt it for use in our DR study. The method is formulated in such a way that it can be easily switched between a full and BOA approach within the box. A highly useful quality is that when using the full solution the results are exact (if converged) and can also serve as a benchmark for all the other DR computations for a given model. Compared to the first 2D FEM-DVR-ECS method this one is harder to implement but much faster and does not suffer from the "energy windows of unconverged Rydbergs" (see e.g. Fig. 2.1).

3.1 The full treatment

Looking back to Fig. 1.2 let us denote the reaction zone $\mathcal{V}$, the electronic fragmentation surface $\mathcal{S}_\mathrm{e}$ and the nuclear fragmentation surface $\mathcal{S}_\mathrm{n}$ (joined, the surfaces are $\mathcal{S}$). The boundaries r_0, R_0 are still chosen such that the Eqs. (1.6), (1.7), (1.8) hold with a high accuracy. We then take the full 2D Hamiltonian Eq. (1.1) and define a rescaled nuclear coordinate $X = R\sqrt{M}$ (and also $X_0 = R_0\sqrt{M}$). The Schrödinger equation (2.1) is altered to

$$\left[H_\mathrm{n}(X) + H_\mathrm{e}(r) + V\left(\frac{X}{\sqrt{M}}, r\right) - E\right]\psi(X, r) = 0\,, \tag{3.1}$$

where

$$H_\mathrm{n}(X) = -\frac{1}{2}\frac{\partial^2}{\partial X^2} + V_0\left(\frac{X}{\sqrt{M}}\right)\,. \tag{3.2}$$

For simplicity we will denote the potentials as $V(X, r)$ and $V_0(X)$. The expression (3.1) is a more symmetric Schrödinger equation which formally describes two interacting distinguishable particles with electronic mass. This means that the eigenvalues $b(E)$ of the two-particle logderivative operator $\mathcal{B}(E)$ satisfy the following variational principle [25]:

$$b(E) = 2\operatorname*{stat}_{\psi}\left\{\frac{\langle\psi|\bar{H} - E|\psi\rangle}{(\psi|\psi)}\right\}\,, \tag{3.3}$$

where we define a symmetrized Hamiltonian $\bar{H}$ via Bloch operators as

$$\bar{H} = H + \frac{1}{2}\left[\delta(X - X_0)\frac{\partial}{\partial X} + \delta(r - r_0)\frac{\partial}{\partial r}\right] , \tag{3.4}$$

$$H = H_{\rm n}(X) + H_{\rm e}(r) + V(X, r) , \tag{3.5}$$

with $\langle\psi|\psi\rangle$ representing a scalar product in the reaction volume $\mathcal{V} = \langle 0, X_0\rangle \times \langle 0, r_0\rangle$ and $(\psi|\psi)$ denoting a scalar product on the fragmentation surface $\mathcal{S}$. By defining $\delta(\mathcal{S}) = \delta(X - X_0) + \delta(r - r_0)$ we can also write

$$(\psi|\psi) = \langle\psi|\delta(\mathcal{S})|\psi\rangle . \tag{3.6}$$

The variational expression (3.3) leads to a Schrödinger equation for the eigenvalues $b_\alpha(E)$

$$2\left(\bar{H} - E\right)|\psi_\alpha\rangle = b_\alpha\,|\psi_\alpha) = b_\alpha\,\delta(\mathcal{S})|\psi_\alpha\rangle . \tag{3.7}$$

The logderivative operator $\mathcal{B}(E)$ and its inverse $\mathcal{R}(E) = \mathcal{B}^{-1}(E)$ operate on functions defined on the surface $\mathcal{S}$. When acting upon functions obtained from surface values of solutions $\psi(X, r)$ of (3.1), the operators are hermitian [25]. The functions $\psi_\alpha(X, r)$ are those solutions of (3.1) that also have a common outward normal logarithmic derivative b_α on the entire surface $\mathcal{S}$. With them we can formally decompose the operators $\mathcal{B}(E)$ and $\mathcal{R}(E)$

$$\mathcal{B} = \sum_\alpha |\psi_\alpha)\, b_\alpha\, (\psi_\alpha| , \tag{3.8}$$

$$\mathcal{R} = \sum_\alpha |\psi_\alpha)\, b_\alpha^{-1}\, (\psi_\alpha| . \tag{3.9}$$

Since the $\delta(\mathcal{S})$ operator on the rhs of (3.7) lowers rank, the equation will generally have many trivial ($b_\alpha = 0$) solutions [24]. These need to be omitted from (3.9) for obvious reasons.

Let us now define a physically motivated orthonormal basis of channels on the fragmentation surface $\mathcal{S}$. The basis can be constructed from two sets of functions. First, on the surface $\mathcal{S}_{\rm e}$ we define $\phi_{j_{\rm e}}$

$$H_{\rm n}(X)\phi_{j_{\rm e}}(X) = E_{j_{\rm e}}\phi_{j_{\rm e}}(X) , \tag{3.10}$$

and second, on the surface $\mathcal{S}_{\rm n}$ we define $\rho_{j_{\rm n}}$

$$[H_{\rm e}(r) + V(X_0, r)]\,\rho_{j_{\rm n}}(r) = E_{j_{\rm n}}\rho_{j_{\rm n}}(r) . \tag{3.11}$$

We then assemble the fragmentation channel basis $|j)$ on the entire surface $\mathcal{S}$ by uniting the two sets ($j = \{j_{\rm e}, j_{\rm n}\}$)

$$j \in j_{\rm e} : \ |j) = |\phi_{j_{\rm e}}) \text{ on } \mathcal{S}_{\rm e} \text{ and } |j) = 0 \text{ on } \mathcal{S}_{\rm n} , \tag{3.12}$$

$$j \in j_{\rm n} : \ |j) = |\rho_{j_{\rm n}}) \text{ on } \mathcal{S}_{\rm n} \text{ and } |j) = 0 \text{ on } \mathcal{S}_{\rm e} . \tag{3.13}$$

In the present study we chose the channel functions to be continuous on $\mathcal{S}$, which leads to the boundary conditions $\phi_{j_{\rm e}}(X_0) = 0$ and $\rho_{j_{\rm n}}(r_0) = 0$. With this surface basis we can now define the R matrix as matrix elements of the $\mathcal{R}$ operator in the fragmentation channel basis. We get the eigenchannel expression

$$R_{jj'} = (j|\mathcal{R}|j') = \sum_\alpha (j|\psi_\alpha)\, b_\alpha^{-1}\, (\psi_\alpha|j') . \tag{3.14}$$

An alternative form of this equation is the Wigner-Eisenbud expansion [26]

$$R_{jj'} = \frac{1}{2}\sum_p \frac{(j|\psi_p)\,(\psi_p|j')}{E_p - E} \ , \tag{3.15}$$

where the eigenstates $|\psi_p\rangle$ and eigenvalues E_p are defined by

$$\bar{H}|\psi_p\rangle = E_p|\psi_p\rangle \ . \tag{3.16}$$

More details about the resolvent form (not discussed here) of the R matrix and the Wigner-Eisenbud expansion can be found in Ref. [B]. The form (3.15) is the most convenient when we need to evaluate the R matrix for many different total energies E. There is an important difference between the eigenstates $|\psi_\alpha\rangle$ and $|\psi_p\rangle$. First, $|\psi_\alpha\rangle$ solve the Schrödinger equation (3.1) for a given total energy E while $|\psi_p\rangle$ satisfy this equation only for discrete $E = E_p$. Second, these two sets have different boundary conditions on the surface $\mathcal{S}$ and so they can differ even with the choice $E = E_p$.

An R matrix computed this way has indices in both open and closed outgoing channels. Due to our choice of $\phi_{j_\mathrm{e}}(X_0) = 0$ and $\rho_{j_\mathrm{n}}(r_0) = 0$ we automatically omit the dissociative scattering in which $r \to \infty$ and $R \to \infty$ simultaneously and so we only have to worry about one-particle asymptotics. Once again, the MQDT technique is employed to eliminate closed channels. Let us first assume that we have N_e channel functions $\phi_{j_\mathrm{e}}(X)$ on the electronic surface $\mathcal{S}_\mathrm{e}$ and N_n channel functions $\rho_{j_\mathrm{n}}(r)$ on the nuclear surface $\mathcal{S}_\mathrm{n}$. Since the full 2D Hamiltonian is separable outside the reaction volume $\mathcal{V}$, the outer region solutions are formed as linear combinations of products of channel functions and asymptotic solutions[5]. For the electronic fragmentation surface we use the real Coulomb functions $f_{j_\mathrm{e}}(r), g_{j_\mathrm{e}}(r)$ defined in the previous chapter. For the nuclear fragmentation surface we use zero-field s-wave radial solutions $F^0_{j_\mathrm{n}}(X), G^0_{j_\mathrm{n}}(X)$ with the following asymptotic behavior

$$F^0_{j_\mathrm{n}}(X) \to \ \ (2/\pi)^{1/2} K_{j_\mathrm{n}}^{-1} \sin(K_{j_\mathrm{n}} X) \ , \tag{3.17}$$

$$G^0_{j_\mathrm{n}}(X) \to -(2/\pi)^{1/2} \cos(K_{j_\mathrm{n}} X) \ , \tag{3.18}$$

for positive $\epsilon_{j_\mathrm{n}} = E - E_{j_\mathrm{n}} = K^2_{j_\mathrm{n}}/2$ and

$$F^0_{j_\mathrm{n}}(X) \to \ \ (1/2\pi)^{1/2} \kappa_{j_\mathrm{n}}^{-1} \left(e^{\kappa_{j_\mathrm{n}} X} - e^{-\kappa_{j_\mathrm{n}} X}\right) \ , \tag{3.19}$$

$$G^0_{j_\mathrm{n}}(X) \to -(1/2\pi)^{1/2} \left(e^{\kappa_{j_\mathrm{n}} X} + e^{-\kappa_{j_\mathrm{n}} X}\right) \ , \tag{3.20}$$

for negative $\epsilon_{j_\mathrm{n}} = -\kappa^2_{j_\mathrm{n}}/2$. If we construct diagonal matrices $\underline{\mathcal{F}}, \underline{\mathcal{G}}$ on the whole surface $\mathcal{S}$ as

$$\underline{\mathcal{F}} \ = \ \mathrm{diag}\left[f_1(r_0), \ldots, f_{N_\mathrm{e}}(r_0), F^0_1(X_0), \ldots, F^0_{N_\mathrm{n}}(X_0)\right] \ , \tag{3.21}$$

$$\underline{\mathcal{G}} \ = \ \mathrm{diag}\left[g_1(r_0), \ldots, g_{N_\mathrm{e}}(r_0), G^0_1(X_0), \ldots, G^0_{N_\mathrm{n}}(X_0)\right] \ , \tag{3.22}$$

[5]The R matrix itself is a general quantity independent of solutions in the outer region. Its application to a model with the interaction of an ion and an electron is given by our specific choice of asymptotic solutions.

then the relation between the R matrix of (3.15) and short-range reaction matrix $\underline{K}$ takes the familiar form

$$\underline{K} = \left(\underline{\mathcal{F}} - \underline{\mathcal{F}}'\underline{R}\right)\left(\underline{\mathcal{G}} - \underline{\mathcal{G}}'\underline{R}\right)^{-1} \ . \tag{3.23}$$

The independent solutions in the fragmentation regions are now

$$\psi_{j'}(X,r) = \sum_{j_{\rm e}=1}^{N_{\rm e}} \phi_{j_{\rm e}}(X)\left[f_{j_{\rm e}}(r)\delta_{j_{\rm e}j'} - g_{j_{\rm e}}(r)K_{j_{\rm e}j'}\right] \tag{3.24}$$

$$+ \sum_{j_{\rm n}=1}^{N_{\rm n}} \rho_{j_{\rm n}}(r)\left[F^0_{j_{\rm n}}(X)\delta_{j_{\rm n}j'} - G^0_{j_{\rm n}}(X)K_{j_{\rm n}j'}\right] \ , \tag{3.25}$$

and they still contain exponentially growing terms in the closed channels. In the R-matrix approach study we used the eigenchannel representation channel elimination technique [27, 28, 6] (as opposed to the short-range S-matrix channel elimination of our FT study [A]). In this case we diagonalize the K matrix

$$K_{jj'} = \sum_{\gamma} U_{j\gamma}\tan(\pi\tau_\gamma)U^\dagger_{\gamma j'} \ , \tag{3.26}$$

and consider the eigenchannel solutions

$$\psi_\gamma(X,r) = \sum_{j_{\rm e}=1}^{N_{\rm e}}\phi_{j_{\rm e}}(X)U_{j_{\rm e}\gamma}[f_{j_{\rm e}}(r)\cos\pi\tau_\gamma - g_{j_{\rm e}}(r)\sin\pi\tau_\gamma]$$

$$+ \sum_{j_{\rm n}=1}^{N_{\rm n}} \rho_{j_{\rm n}}(r)U_{j_{\rm n}\gamma}\left[F^0_{j_{\rm n}}(X)\cos\pi\tau_\gamma - G^0_{j_{\rm n}}(X)\sin\pi\tau_\gamma\right] \ , \tag{3.27}$$

where $\pi\tau_\gamma$ is the eigenphase common for all the electronic and nuclear fragmentation channels [29]. We then search for a coefficient set A_γ such that the combination

$$\psi(X,r) = \sum_\gamma \psi_\gamma A_\gamma \tag{3.28}$$

decays exponentially in all the closed channels and has the same physical eigenphase shift δ on the surface $\mathcal{S}$ in all the open channels. Following previous Coulomb and free-field procedures [28, 6], $N^{\rm o}_{\rm e}$ and $N^{\rm o}_{\rm n}$ denote the number of open channels on the electronic and nuclear surfaces respectively. It is known (Ref. [24]) that there are at most $N^{\rm o}_{\rm e} + N^{\rm o}_{\rm n}$ independent coefficient sets A_γ, such that the exponential growth is cancelled in Eq. (3.28). We denote them with a second index $A_{\gamma\rho}$. Let us define matrices $\underline{\Gamma}$ and $\underline{\Lambda}$

$$\Gamma_{j\gamma} = \begin{cases} U_{j\gamma}\sin(\beta_j + \pi\tau_\gamma) \ , & j \in Q_{\rm e} \\ U_{j\gamma}\left(\kappa_j^{-1}\cos\pi\tau_\gamma + \sin\pi\tau_\gamma\right) \ , & j \in Q_{\rm n} \\ & \\ U_{j\gamma}\sin\pi\tau_\gamma \ , & j \in P_{\rm e} \\ U_{j\gamma}K_j^{1/2}\sin\pi\tau_\gamma \ , & j \in P_{\rm n} \end{cases} \ , \tag{3.29}$$

$$\Lambda_{j\gamma} = \begin{cases} 0 \ , & j \in Q_{\rm e} \\ 0 \ , & j \in Q_{\rm n} \\ & \\ U_{j\gamma}\cos\pi\tau_\gamma \ , & j \in P_{\rm e} \\ U_{j\gamma}K_j^{-1/2}\cos\pi\tau_\gamma \ , & j \in P_{\rm n} \end{cases} \ , \tag{3.30}$$

where $Q_\mathrm{e}, Q_\mathrm{n}$ denote sets of closed electronic and nuclear channels and $P_\mathrm{e}, P_\mathrm{n}$ are sets of open electronic and nuclear channels. The coefficients K_j, κ_j are the same as in (3.17) and (3.19) and β_j is again the effective closed-channel quantum number (2.17). The matrices $\underline{\Gamma}, \underline{\Lambda}, \underline{A}, \underline{\delta}$ satisfy[6]

$$\underline{\Gamma}\,\underline{A} = \underline{\Lambda}\,\underline{A}\tan\underline{\delta}\;, \tag{3.31}$$

which is a singular generalized eigenvalue problem for unknown $A_{\gamma\rho}$ and δ_ρ. After solving this we can determine the energy-normalized physical solutions

$$\psi_\rho(X,r) = \sum_{j\in P_\mathrm{e}} \phi_j(X) T_{j\rho}\left[f_j(r)\cos\pi\delta_\rho - g_j(r)\sin\pi\delta_\rho\right] \tag{3.32}$$

$$+ \sum_{j\in P_\mathrm{n}} \rho_j(r) T_{j\rho}\left[F_j(X)\cos\pi\delta_\rho - G_j(X)\sin\pi\delta_\rho\right]\;, \tag{3.33}$$

with the transformation matrix $\underline{T}$

$$T_{j\rho} = \sum_\gamma A_{\gamma\rho}\left(\Lambda_{j\gamma}\cos\pi\delta_\rho + \Gamma_{j\gamma}\sin\pi\delta_\rho\right)\;. \tag{3.34}$$

The physical scattering matrix is then

$$S^\mathrm{phys}_{jj'} = \sum_\rho T_{j\rho} e^{2i\delta_\rho} T_{j'\rho}\;, \quad j,j' \in P_\mathrm{e}\cup P_\mathrm{n}\;, \tag{3.35}$$

and the DR cross section

$$\sigma^\mathrm{DR}_{j\leftarrow j'} = \frac{\pi}{2\epsilon'_j}|S^\mathrm{phys}_{jj'}|^2\;, \quad j\in P_\mathrm{n}\;, j'\in P_\mathrm{e}\;. \tag{3.36}$$

If we want to compute vibrational excitation we simply choose the outgoing channel on the electronic fragmentation surface instead

$$\sigma^\mathrm{VE}_{j\leftarrow j'} = \frac{\pi}{2\epsilon'_j}|S^\mathrm{phys}_{jj'} - \delta_{jj'}|^2\;, \quad j,j'\in P_\mathrm{e}\;. \tag{3.37}$$

As a sidenote to this approach, despite the visual representation of Fig. 1.3, the electronic box size for this full approach is in practice noticeably larger than the r_0 value in the frame transformation computations. This is due to the fact that now we actually need to explicitly compute the functions $\rho_{j_\mathrm{n}}(r)$ of (3.11) in all the open and weakly closed channels. To properly represent them while satisfying the boundary condition $\rho_{j_\mathrm{n}}(r_0) = 0$ we need a sizeable electronic box (still much smaller than the 2D FEM-DVR-ECS method of section 1.2). In our second study computations we used $r_0 = 50$ bohr and $R_0 = 15$ bohr.

3.2 Born-Oppenheimer variant

The BOA version of the 2D R-matrix approach follows the same steps with a few adjustments. We split the symmetrized Hamiltonian of Eq. (3.4) into its respective nuclear and electronic parts (without the interaction V)

$$\bar{H}_\mathrm{n}(X) = H_\mathrm{n}(X) + \frac{1}{2}\delta(X-X_0)\frac{\partial}{\partial X}\;, \tag{3.38}$$

$$\bar{H}_\mathrm{e}(r) = H_\mathrm{e}(r) + \frac{1}{2}\delta(r-r_0)\frac{\partial}{\partial r}\;. \tag{3.39}$$

[6] $\underline{\delta}$ is now a diagonal matrix of all physical eigenphase shifts.

We can then define fixed-nuclei electronic solutions as

$$\left[\bar{H}_{\rm e}(r) + V(X,r)\right] \Psi_k^{\rm BO}(r;X) = \bar{E}_k(X)\Psi_k^{\rm BO}(r;X) \ , \tag{3.40}$$

where X is now used as a parameter. With this we also define nuclear functions $\phi_{kp}(X)$ solving the decoupled nuclear Schrödinger equations

$$\left[\bar{H}_{\rm n}(X) + \bar{E}_k(X)\right] \phi_{km}^{\rm BO}(X) = E_m \phi_{km}^{\rm BO}(X) \ . \tag{3.41}$$

In a full treatment the previous equation would contain additional coupling terms on the rhs

$$\left[\bar{H}_{\rm n}(X) + \bar{E}_k(X) - E_m\right] \phi_{km}(X) = -\frac{1}{2}\sum_{k'} \left[V_{kk'}^{(1)}(X) + V_{kk'}^{(2)}(X)\right] \phi_{k'm}(X) \ , \tag{3.42}$$

where

$$V_{kk'}^{(1)}(X) = \left|\frac{\partial}{\partial X}\right\rangle \langle\psi_k|\psi'_{k'}\rangle_r + \langle\psi'_k|\psi_{k'}\rangle_r \left\langle\frac{\partial}{\partial X}\right| \ , \tag{3.43}$$

$$V_{kk'}^{(2)}(X) = \langle\psi'_k|\psi'_{k'}\rangle_r \ , \tag{3.44}$$

and where $\psi'_k = \partial\psi_k(r;X)/\partial X$ and the product $\langle .|.\rangle_r$ is carried out only in the electronic coordinate r. In the BOA the coupling is neglected and the full wave function is just the simple

$$\psi_p^{\rm BO}(X,r) = \Psi_k^{\rm BO}(r;X)\phi_{km}^{\rm BO}(X) \ , \tag{3.45}$$

where $p \equiv \{k,m\}$ represents a combined index of the electronic states (indexed by k) and the nuclear states (indexed by m). The BOA R matrix is then

$$R_{jj'}^{\rm BO} = \frac{1}{2}\sum_p \frac{(j|\psi_p^{\rm BO})\,(\psi_p^{\rm BO}|j')}{E_p - E} \ , \tag{3.46}$$

which was introduced previously by Schneider *et al.* [8].

The electronic box size r_0 for this approach needs to be smaller than for the full approach in order to have any hope of satisfying the BOA. However, it is difficult to match this small r-box R matrix to the outer channel functions, because the electronic channel functions on the nuclear fragmentation surface may not fit. A possible solution is to propagate the 2D R matrix in the interaction-free region to some larger electronic distance. The R-matrix propagation was previously used by Baluja *et al.* [30] for the one-dimensional case and Scott *et al.* [31] for two indistinguishable particles. Our version for two distinguishable particles can be found in the appendix of Ref. [B].

After computing the BOA R matrix and propagating it to a larger electronic distance, the remaining steps towards computing the cross sections are the same as in the full treatment. In summary, it is the transformation of $\underline{R}$ into $\underline{K}$ (3.23), diagonalization of $\underline{K}$ into $\tan\pi\tau_\gamma$ and $U_{j\gamma}$, finding the solution of (3.31) and applying (3.34), (3.35) and (3.36) or (3.37).

We should also emphasize again that in the same way as was the case in the FT method, this approach only ever assumes BOA in some restricted short-range region defined by the extent of the electronic interaction and uses analytical Schrödinger equation solutions for long ranges. Thus, we assume that any conclusions about the validity of the BOA in this method will be relevant to the limitations of the frame transformation.

3.3 2D R-matrix insights

Upon implementation, the converged results of the full R-matrix method are just as accurate as the results of the 2D FEM-DVR-ECS approach (where it is converged) and they do not suffer from the unconverged energy windows. Because of this advantage, we have chosen to use them as the exact results in comparisons going forward. As stated earlier the electronic box size of the full method was $r_0 = 50$ bohr to properly represent the relevant electronic states on the nuclear fragmentation surface. We tested the validity of the BOA approach for three sizes of the smaller box $r_0 = 6$ bohr, 12 bohr and 20 bohr (always propagating the R matrix up to the full 50 bohr afterwards), with 6 bohr being the smallest possible distance still confining the interaction $V(R, r)$. As expected the validity of BOA quickly deteriorates for increasing electronic box sizes as shown in Figs 3.1 and 3.2. The index n is now used to denote the outgoing Rydberg channels.

The impact of the first-order nonadiabatic coupling $V^{(1)}_{kk'}(X)$ can be easily deduced from Figs. 3.3 and 3.4. Seeing as the poles get much denser for increasing electronic box size while the terms $\langle\psi'_k|\psi_{k'}\rangle_r$ stay on the same order of magnitude the coupling will bear an increasingly large impact on (3.42) as its strength becomes comparable with the spacing of the R-matrix poles.

The BOA results for the box size of 6 bohrs are quite close to the correct value and enhancing them with the first order correction makes them visually indistinguishable from the exact results. For the larger box sizes Figs. 3.5 and 3.6 show the improvement brought by including the first correction. A comparison for inelastic vibrational excitation cross sections is also interesting and is shown in Fig. 3.7. It is clear that the deterioration of BOA has a much smaller impact on the VE cross sections.

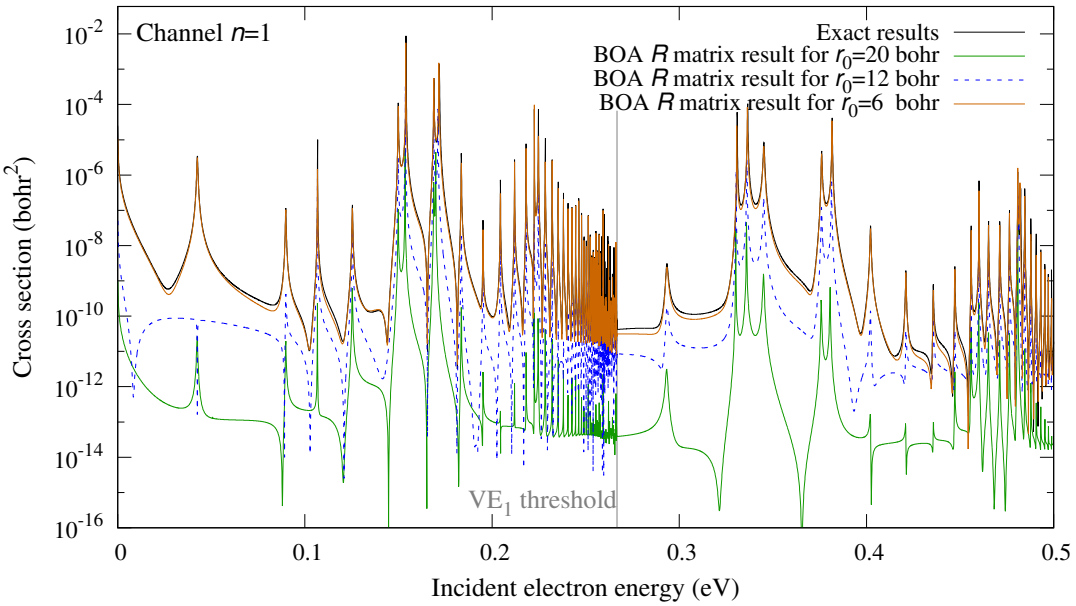

Figure 3.1: DR cross sections into the $n = 1$ lowest open Rydberg channel. The black curve is the full method exact result and the rest are BOA results for $r_0 = 6$ bohr, 12 bohr and 20 bohr. Remember that this channel is unphysical (a detailed discussion can be found under Eq. (1.5)).

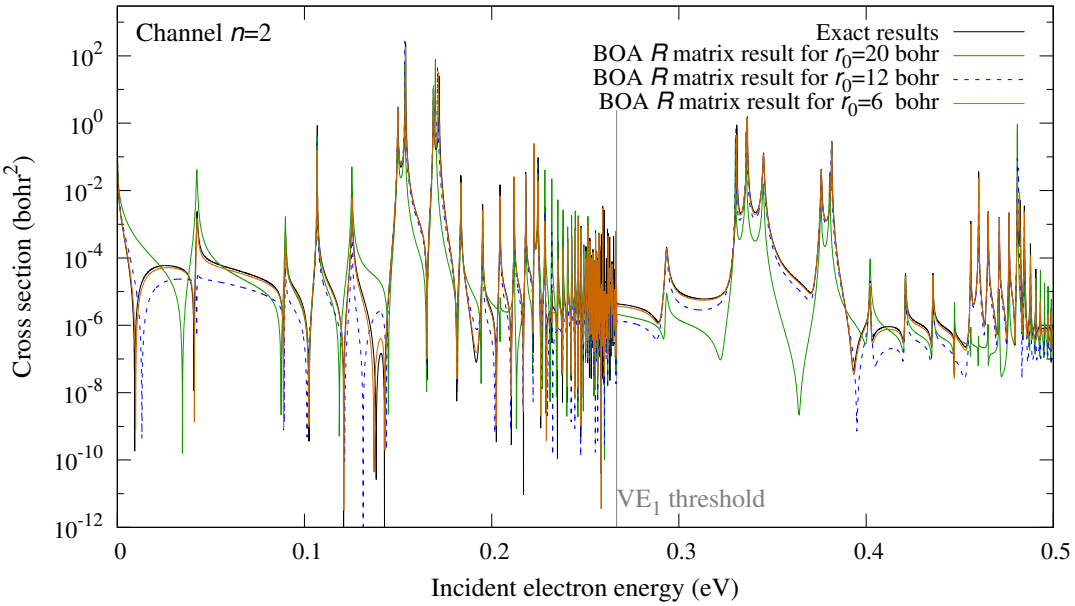

Figure 3.2: DR cross sections into the $n = 2$ Rydberg channel. The black curve is the full method exact result and the rest are BOA results for $r_0 = 6$ bohr, 12 bohr, and 20 bohr.

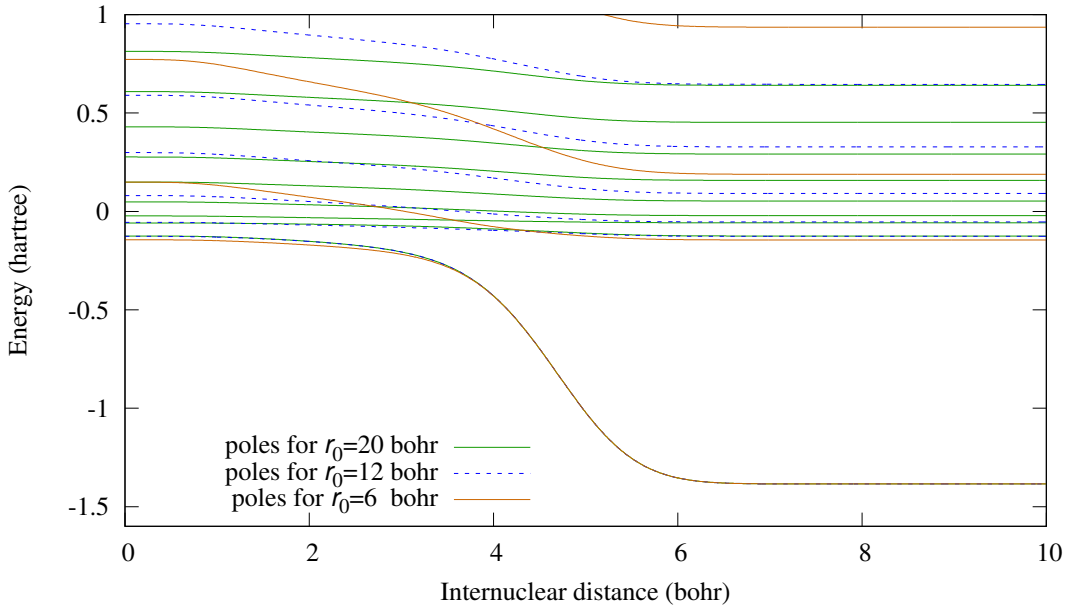

Figure 3.3: Poles $\bar{E}_k(R)$ (3.40) of the fixed-nuclei R matrix as functions of internuclear distance for three sizes of the BOA box r_0.

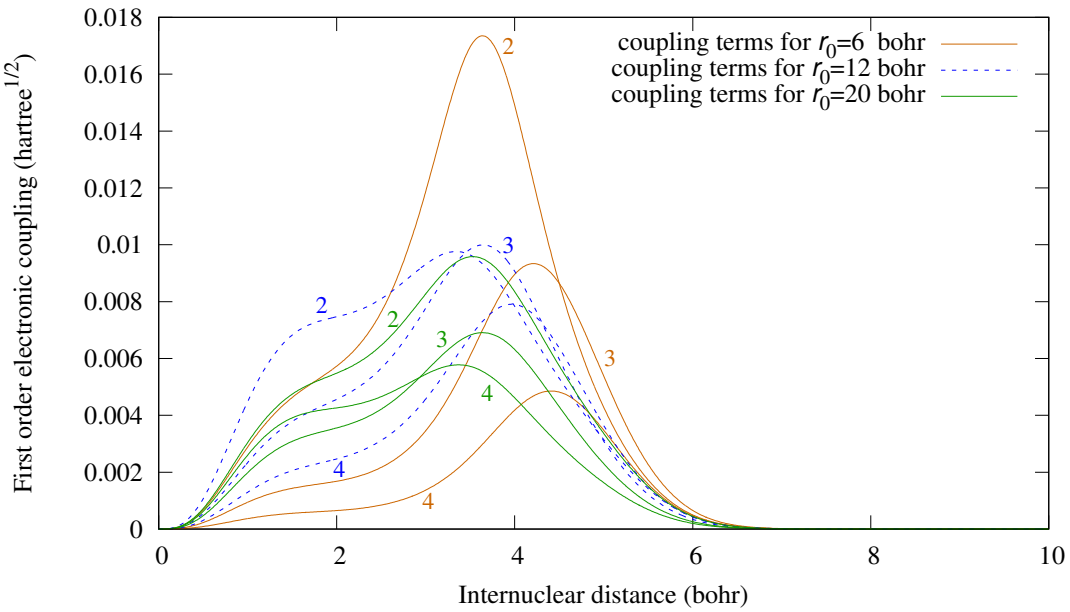

Figure 3.4: First order electronic coupling terms $\langle \psi'_k | \psi_{k'} \rangle_r$ of (3.43) for $k' = 1$ and $k = 2, 3, 4$ (denoted by numbers next to curves) and for the three box sizes.

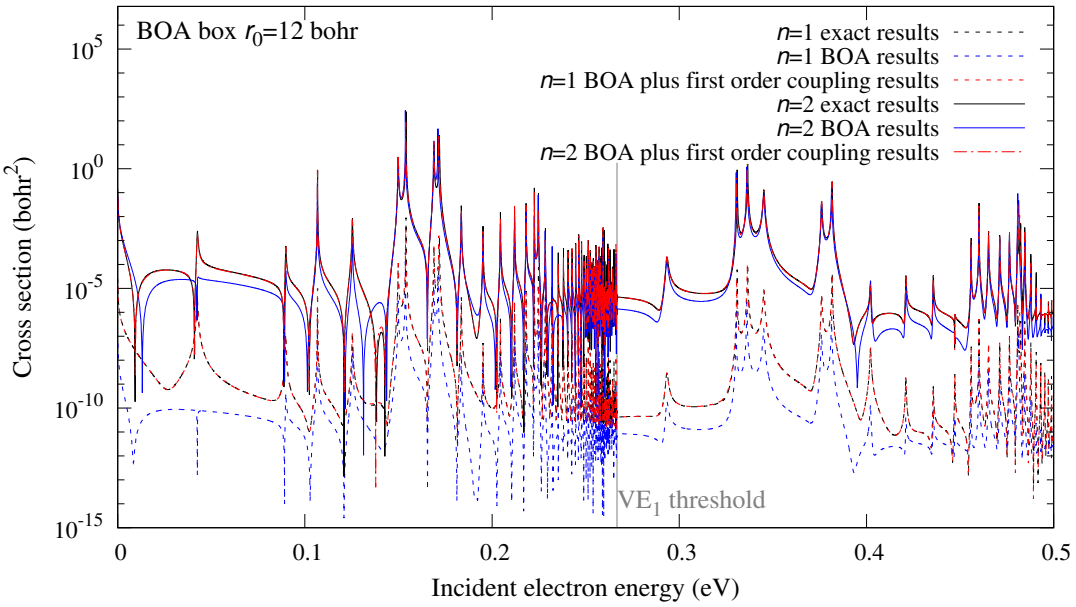

Figure 3.5: DR cross sections into the $n = 1$ (dashed curves) and $n = 2$ (solid and dot-dashed curves) channels. The black curves are exact results the blue curves are BOA results for $r_0 = 12$ bohr and red curves are BOA with first order couplings (also for $r_0 = 12$ bohr).

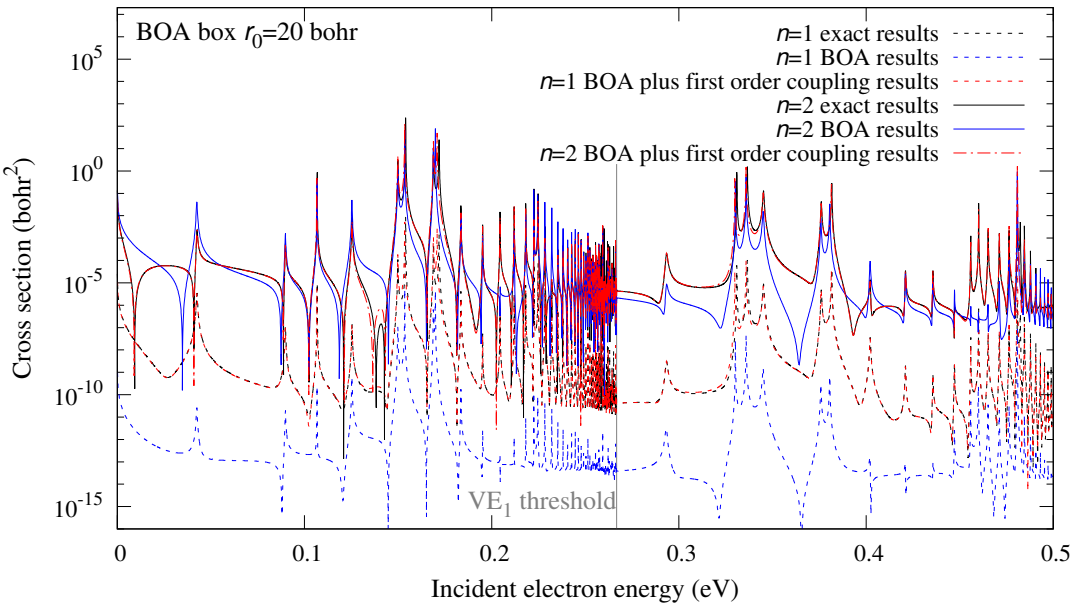

Figure 3.6: Same as Fig. 3.5 but with $r_0 = 20$ bohr instead.

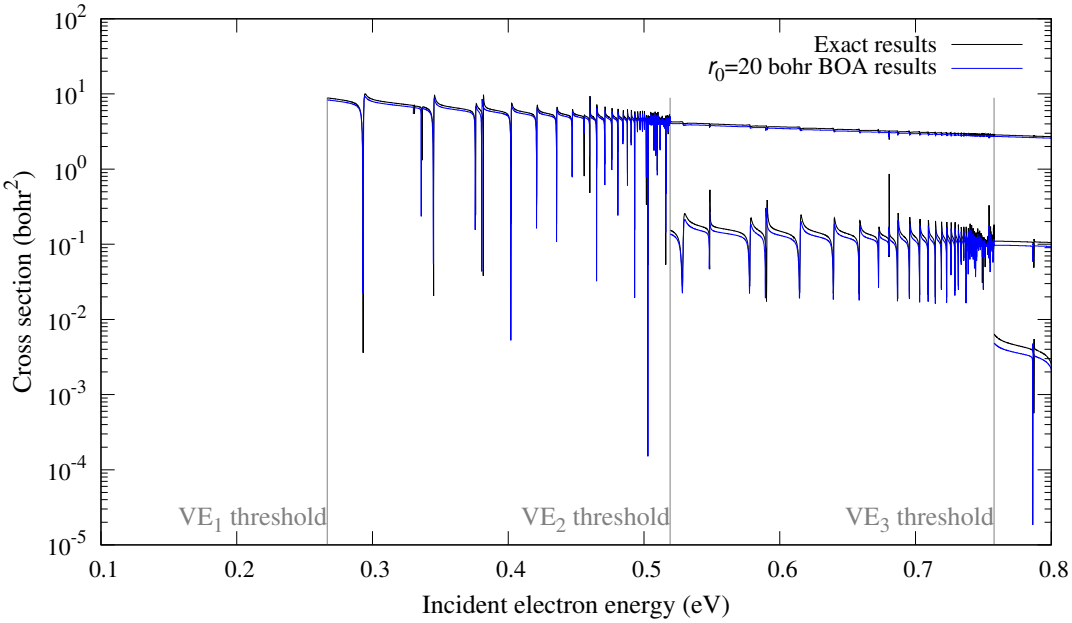

Figure 3.7: Inelastic VE cross sections into the first three channels comparing the exact results (black curves) with the BOA results, $r_0 = 20$ bohr (blue curves).

4. Improvements of our theoretical toolkit

The 2D R-matrix study has provided us with improved results that do not suffer from the same convergence problems as the original benchmark model and thus serve as the new "exact results" to compare against. It has also shown that the BOA might actually be too strong of an assumption within the electronic box sizes that we have chosen previously. The artificial quantum defect shift tests of the first FT study (see Fig. 2.4) have shown that the various simplifying assumptions regarding energy independence implemented in the theoretical derivation can have a visible impact on the results. Finally, the Siegert pseudo-states form a basis with various issues that also need to be addressed. The following sections detail how our second FT study [C] (third DR study overall) tackled these various issues in an attempt to improve the FT theory approach when applied to the DR process.

4.1 Vibrational basis selection

To rectify the completeness issues of the Siegert pseudo-state basis (section 2.3), in our second FT study, we switched to exterior complex scaling (ECS) to form the nuclear vibrational basis. It is based on solving the nuclear vibrational Hamiltonian on a bent complex contour Z following

$$Z = \begin{cases} R \,, & \text{for } R \leq R_0 \,, \\ R_0 + \mathrm{e}^{i\theta}(R - R_0) \,, & \text{for } R_0 < R \leq R_m \,, \end{cases} \tag{4.1}$$

where R is the real parameter (length) of the nuclear coordinate, $R_0 = Z_0$ is the ECS bending point, θ is the ECS bending angle, and R_m parametrizes the end of the contour Z_m. Generally, solving

$$H_{\mathrm{n}}(Z)\phi_{j'}(Z) = E_{j'}\phi_{j'}(Z) \,, \tag{4.2}$$

with the correct choice of θ, while imposing a zero value boundary condition at Z_m, yields states that behave as bound or outgoing-wave continuum states for $0 < Z < Z_0$. For a well behaved Hamiltonian, in order to get outgoing-wave eigenstates with well behaved eigenenergies the bending angle θ needs to be between 0° and 45° and the expert reader will notice that whenever the nuclear Hamiltonian contains a potential with terms proportional to higher powers of R one might need to constrain the contour angle further. ECS basis orthogonality relations are quite simple

$$\int_0^{Z_m} \phi_j(Z)\phi_{j'}(Z)\mathrm{d}Z = \delta_{jj'} \,, \tag{4.3}$$

or equivalently along the real parameter R

$$\int_0^{R_m} \phi_j(R)\phi_{j'}(R)q(R)\mathrm{d}R = \delta_{jj'} \,, \tag{4.4}$$

with

$$q(R) = \begin{cases} 1\ , & \text{for } R \leq R_0\ , \\ \mathrm{e}^{i\theta}\ , & \text{for } R > R_0\ . \end{cases} \tag{4.5}$$

The Eqs. (4.3) or (4.4) also define normalization (equivalently). Fig. 4.1 shows the spectrum of such ECS states compared with the bound and outgoing-wave parts of the Siegert pseudo-state spectrum computed using the same nuclear Hamiltonian (1.2) with $R_0 = 15$ bohr, $R_m = 40$ bohr and $\theta = 40°$. The outgoing waves computed on an ECS grid split into three branches:

- States that oscillate on the real part of the contour and decay exponentially on the complex part. Curiously, if we set the bending point R_0 of (4.1) to be equal to the point of the Siegert boundary condition (2.7) R_0 and use the normalization of (4.3), these states' momenta will coincide with the Siegert pseudo-state outgoing-wave momenta, as is apparent in Fig. 4.1. Furthermore, their corresponding wave functions are also identical on the interval $0 < R < R_0$ as is shown in Fig 4.2. This means that two different sets of states (Siegert and ECS), with two different normalizations (2.8) and (4.3) yield equal eigenstates on the real coordinate axis. Therefore, the surface term in the Siegert normalization (2.8) represents the ECS normalization integral (4.3) over the bent part of the complex contour.
- States, that are almost zero on most of the real part, then rise sharply at R_0 and continue to oscillate with an almost constant amplitude on the interval $R_0 < Z < Z_m$. They reach a node at Z_m and thus behave like box states. Their complex momenta lie almost exactly at the $-\theta$ line.
- A few states with momenta close to zero. Their wave functions behave as a mixture of the previous two categories (oscillatory with exponential amplitude changes on both parts of the contour).

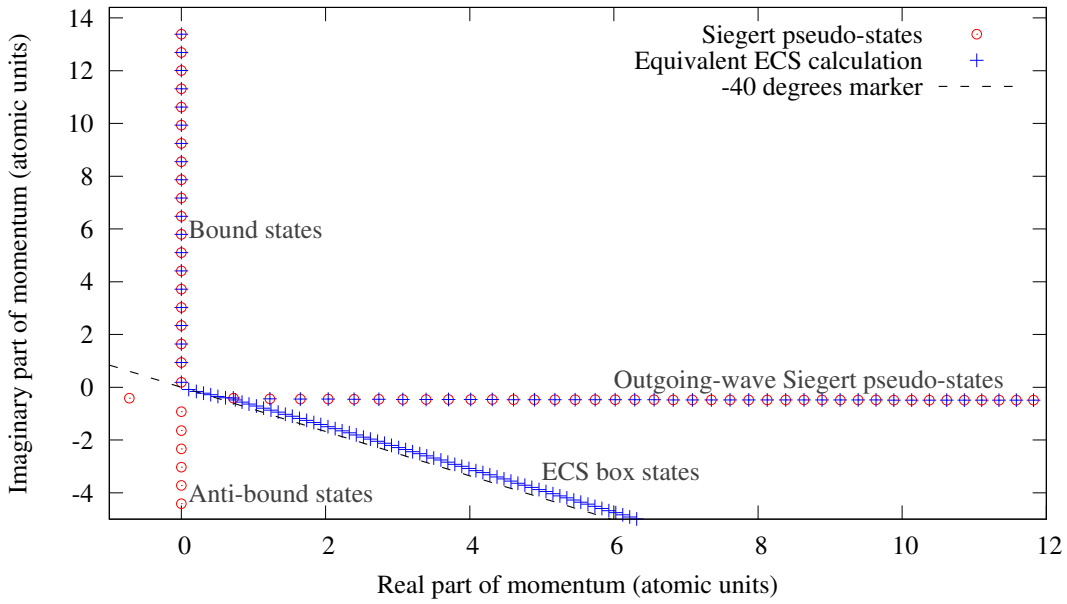

Figure 4.1: Siegert pseudo-state and ECS state complex eigenmomenta example.

For further details on the ECS see C. W. McCurdy's and F. Martín's paper [32].

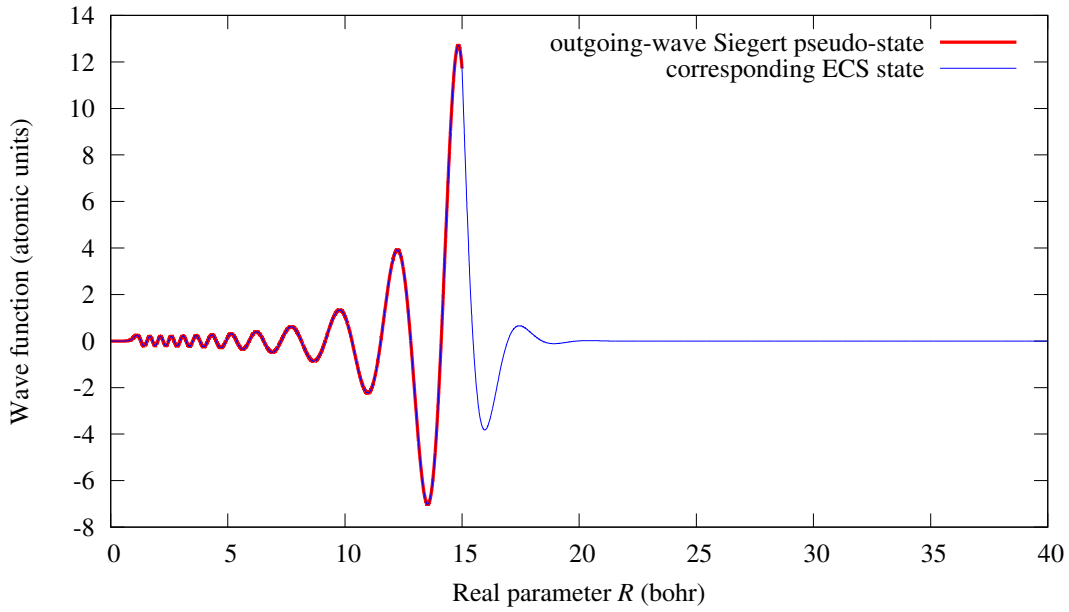

Figure 4.2: Comparison of a selected outgoing-wave Siegert pseudo-state wave function and the corresponding ECS basis wave function.

The change from Siegert pseudo-states to ECS states corrected the computed cross sections in certain small energy windows (typically around DR channel openings) and also simplified some parts of the implementation. The frame transformation functional is now

$$F_j[h(Z)] = \int_0^{Z_m} \mathrm{d}Z \phi_j(Z) h(Z) \ , \tag{4.6}$$

and so the frame transformed matrices (like e.g. (2.14)) drop the surface term. Overall though, apart from the problematic energy windows, this change alone did not alter the earlier FT results.

4.2 Energy-dependent FT theory

Our naive simulation of the energy dependence of the quantum defect shown in Fig. 2.4, has motivated us to improve the energy-independent theory along the ideas presented by Gao and Greene [7]. The method is mostly analogous to section 2.1 with some key changes.

We start with the same Schrödinger equation (2.1) (replacing R with Z when using ECS) and definitions of vibrational basis and Coulomb functions. In this study, we have chosen to use real asymptotics f, g instead of the complex $f^{\mp}$. Thus, instead of (2.4) the inner-region BOA solution can be written at r_0 as

$$\psi_{j'}(Z, r_0) = \phi_{j'}(Z) N(Z, \epsilon_{j'}) \left[f_{j'}(r_0) \cos\pi\mu(\epsilon_{j'}, Z) - g_{j'}(r_0) \sin\pi\mu(\epsilon_{j'}, Z) \right] \ , \tag{4.7}$$

where the normalization factor $N(Z, \epsilon_{j'})$ is not neglected anymore. It can be computed using only the electronic-surface properties [6, 33]

$$N(Z, \epsilon_{j'}) = \left[\frac{\partial \mu(Z, \epsilon_{j'})}{\partial \epsilon_{j'}} + \frac{1}{2} W(Z, \epsilon_{j'}) \right]^{-1/2} \ , \tag{4.8}$$

with

$$W(Z,\epsilon_{j'}) = \Big([f_{j'},g'_{j'}]+[g_{j'},f'_{j'}]\Big)\sin\pi\mu(Z,\epsilon_{j'})\cos\pi\mu(Z,\epsilon_{j'}) \\ -[f_{j'},f'_{j'}]\cos^2\pi\mu(Z,\epsilon_{j'})-[g_{j'},g'_{j'}]\sin^2\pi\mu(Z,\epsilon_{j'})\ , \qquad (4.9)$$

where $[.,.]$ is again the Wronskian of two functions and $f' \equiv \partial f/\partial\epsilon$. The outer-region solution is now a general linear combination of $\phi_n(Z)f_n(r)$ and $\phi_n(Z)g_n(r)$. We then match the independent BOA solutions (4.7) evaluated at $r = r_0$ with

$$\sum_n \phi_n(Z)\left[f_n(r_0)I_{nj'} - g_n(r_0)J_{nj'}\right]\ . \qquad (4.10)$$

By applying $F_j[\ .\ ]$ to both sides we get

$$f_{j'}(r_0)\mathcal{C}_{jj'} - g_{j'}(r_0)\mathcal{S}_{jj'} = f_j(r_0)I_{jj'} - g_j(r_0)J_{jj'}\ , \qquad (4.11)$$

where

$$\mathcal{C}_{jj'} = \int_0^{Z_m} dZ\,\phi_j(Z)N(Z,\epsilon_{j'})\cos\pi\mu(Z,\epsilon_{j'})\phi_{j'}(Z)\ , \\ \mathcal{S}_{jj'} = \int_0^{Z_m} dZ\,\phi_j(Z)N(Z,\epsilon_{j'})\sin\pi\mu(Z,\epsilon_{j'})\phi_{j'}(Z)\ , \qquad (4.12)$$

are the frame-transformed sine and cosine matrices. We once again apply Wronskians of Coulomb functions to get the coefficient matrices

$$I_{jj'} = \frac{1}{[f_j,g_j]}\left([f_{j'},g_j]\mathcal{C}_{jj'} - [g_{j'},g_j]\mathcal{S}_{jj'}\right)\ , \\ J_{jj'} = \frac{1}{[g_j,f_j]}\left([f_{j'},f_j]\mathcal{C}_{jj'} - [g_{j'},f_j]\mathcal{S}_{jj'}\right)\ . \qquad (4.13)$$

The short-range reaction matrix $\underline{K}$ is then

$$\underline{K} = \underline{J}\underline{I}^{-1}\ . \qquad (4.14)$$

It can be Cayley-transformed into the short-range scattering matrix $\underline{S}$

$$\underline{S} = (1+i\underline{K})\,(1-i\underline{K})^{-1}\ , \qquad (4.15)$$

and the proceeding MQDT closed-channel elimination technique is the same as before (2.16). The computation of cross sections (2.18) is also unchanged.

At first, the direct implementation of energy-dependent FT proved unfruitful as the DR calculations actually yielded strongly decreased accuracy of results when compared to the seemingly inferior energy-independent procedure. The first thing this approach taught us, and which should serve as a letter of caution for anyone attempting to use the full energy-dependent FT theory for DR, is that the implementation can be very sensitive to properties like unitarity, subunitarity and symmetry of various frame transformed matrices within the process. The inclusion of energy-dependent quantum defects, normalization coefficients and Coulomb function Wronskian terms will often make previously symmetric matrices no longer such. Doubly so for someone using a slightly incomplete vibrational basis (in the relevant part of the Hilbert space). This is also the reason why we

switched from complex $f^{\mp}$ asymptotics to real f, g asymptotics and reformulated our approach to compute the frame-transformed K matrix first and then Cayley transform it into the S matrix. In addition and rather vexingly, we found that we needed to artificially symmetrize the short-range K matrix (4.14) before we could proceed to the MQDT channel elimination step. This is rather reminiscent of a K-matrix symmetrization step that was necessary in F. Robicheaux's energy-dependent FT treatment of the dissociative electron attachment to H_2 [34]. In our case without this artificial step the VE cross sections gain a relative error of about $\sim 1\%$ which wholly breaks the accuracy of the "one minus" DR cross-section computation. It is unnecessary only for energies below the first VE threshold where there is only one open channel on the electronic fragmentation surface and the physical S or K matrices are one-by-one and thus automatically symmetric.

4.3 Electronic boundary backpropagation

After solving the K-matrix symmetry problems, the results were still less accurate than the previous energy-independent calculations presented in our first publication [A] (and in chapter 2). Thanks to the 2D R-matrix study of our second publication [B] we knew that our electronic radius of $r_0 = 7$ bohrs (chosen for good convergence of quantum defect values) could already be too large for the BOA to hold. Indeed as Fig. 4.3 shows, the electronic wave function

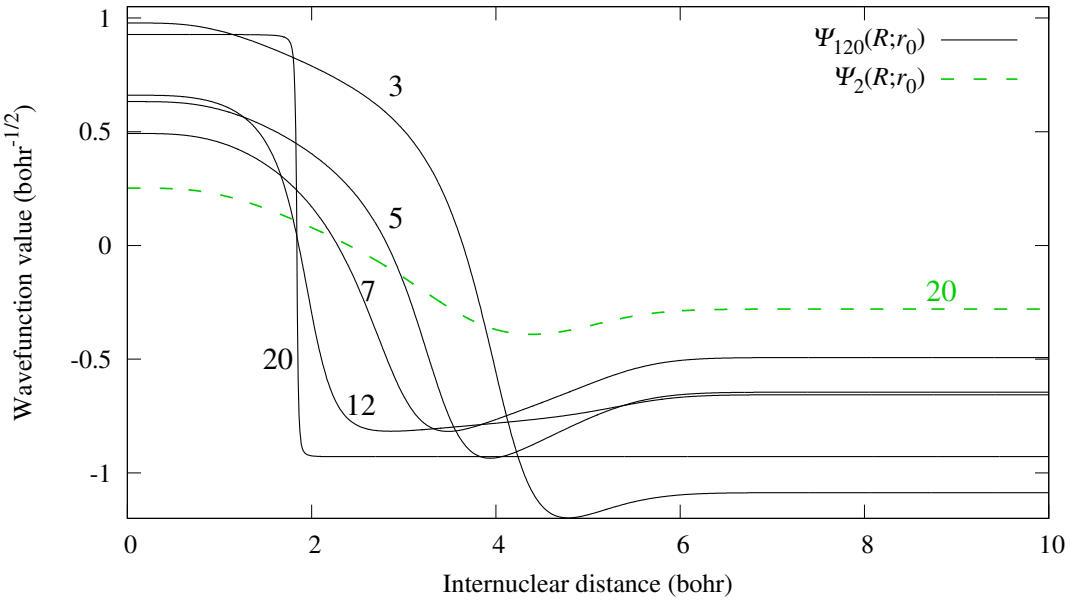

Figure 4.3: The R-dependence of the BOA electronic wave functions $\psi_{j'}(R, r_0)$ at the boundary r_0. The black curves show this for $j' = 120$ (indexing corresponds to ascending real parts of electronic energies) and box sizes $r_0 = 3, 5, 7, 12, 20$ bohr. The red dashed curve shows this for the largest box size and $j' = 2$.

at the boundary r_0 is rather sharply dependent on R for r_0 values of 5 bohrs and above, which increases importance of the first- and second-order correction terms. From these tests stemmed the crucial idea that made the implementation

of the energy-dependent FT method for DR possible. We call it the backpropagated frame transformation and it hinges on finding the correct and converged quantum defect at some larger electronic radius but then on propagating (interaction free) the electronic solution to some smaller electronic radius r_1 where BOA holds.The actual FT procedure is then carried out at r_1 with the quantum defect information obtained at larger r_0. This approach is quite *ad hoc* and has its own limitations (backpropagating too much may cause the wave function normalization to explode) but finally yields much better results than the simple energy-independent method. Without it the full energy-dependent implementation does not work well. Implementation-wise there are no new equations to follow. We simply compute the BOA quantum defects for some larger r_0 value (e.g. 7 bohrs) where they are converged, but then we use a smaller $r_0 \to r_1$ (e.g. 2 bohrs) to compute the normalization (4.8) and the $\underline{I}$, $\underline{J}$ matrices (4.13). The accuracy of these results is shown in Fig. 4.4 and also in Fig. 4.5 along with the accuracy of the following simplified approach.

4.4 Simplified backpropagation

While coming up with the backpropagation solution we have also "stumbled upon" another approach that improves upon the energy-independent results but is simpler to implement than the full backpropagated procedure. If during the backpropagation step $r_0 \to r_1$(small) we again assume that f_j, g_j lose their energy dependence, then Eq. (4.13) simplifies to

$$\begin{aligned} I_{jj'} &= \mathcal{C}_{jj'} \ , \\ J_{jj'} &= \mathcal{S}_{jj'} \ , \end{aligned} \tag{4.16}$$

and $\underline{K} = \underline{\mathcal{S}}\underline{\mathcal{C}}^{-1}$. The normalization factor $N(Z, \epsilon_{j'})$ from (4.12) will not exactly cancel out in $\underline{\mathcal{S}}\underline{\mathcal{C}}^{-1}$ due to right-index energy dependence. If we assume that it does and then redefine $\underline{\mathcal{S}}, \underline{\mathcal{C}}$ accordingly

$$\begin{aligned} \mathcal{C}_{jj'} &= \int_0^{Z_m} dZ \, \phi_j(Z) \cos \pi\mu(Z, \epsilon_{j'}) \phi_{j'}(Z) \ , \\ \mathcal{S}_{jj'} &= \int_0^{Z_m} dR \, \phi_j(Z) \sin \pi\mu(Z, \epsilon_{j'}) \phi_{j'}(Z) \ , \end{aligned} \tag{4.17}$$

then we completely avoid explicit evaluation of both the normalization factor and the Coulomb functions f, g. This also means that no evaluation of any specific electronic radius r_0 or r_1 appears any more in the implementation.

This approach is somewhere in-between the full energy-dependent method and the simple energy-independent method and gives us better understanding of why our direct application of the energy-dependent FT method [7] failed while the energy-independent approach functions much better. The reason for the failure is a poor accuracy of the inner-region BOA solutions (4.7) with high index j' (as we saw in the discussion surrounding Fig. 4.3). The inclusion of these high states is only necessary for the computation of DR cross sections and not VE, which is why previous applications of the energy-dependent FT theory did not suffer from this problem. Now, the math of the simplified energy-dependent approach can be interpreted as actually circumventing any BOA problems by "silently" applying

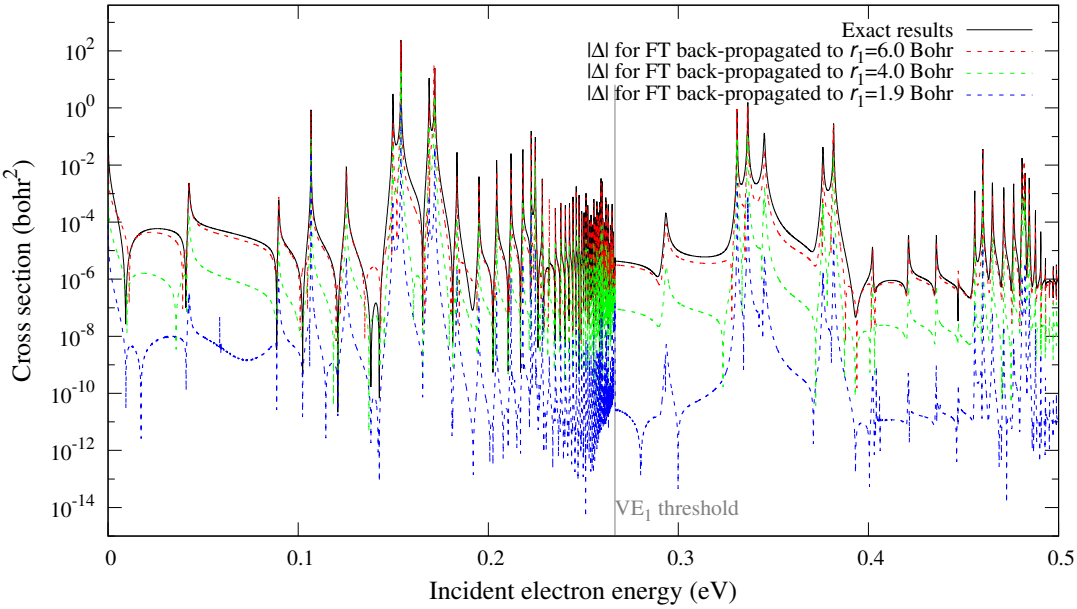

Figure 4.4: Comparison of the DR cross sections for the full backpropagated energy-dependent FT. Since the actual cross-section curves are so similar we instead plot only the exact data (solid black curve) and the absolute values of differences $|\Delta|$ from the exact results (dashed curves). We show results for three different backpropagation radii. Red curve for $r_1 = 6.0$ bohr, green curve for $r_1 = 4.0$ bohr and blue curve for $r_1 = 1.9$ bohr.

$r_0 \to 0$. This also helps us to understand how the original energy-independent method of chapter 2 does not exhibit problems with the BOA. It not only neglects the energy dependence of the quantum defect in (2.14), but it also neglects the entire energy dependence of the inner-region BOA solutions (2.4)[7]. Once again, the energy independence of $f_j^{\mp}(r)$ coupled with the absence of any explicit r_0 in the energy-independent FT formulas, can be seen as "silently" applying $r_0 \to 0$ and circumventing all of the BOA problems.

The simplified backpropagation technique is also equivalent with the simplified energy-dependent FT used to compute vibrational excitation of N_2 by Gao and Greene [7]. A comparison of accuracy for the different methods can be seen in Fig. 4.5. The accuracy is now so high that the error $|\Delta|$ is always within 0.1% or 1% of the exact result for the full and simplified method, respectively. For the sake of completeness we also compare the inelastic VE cross sections in Fig. 4.6. We can see that for the VE process even the non-propagated result (which is catastrophic for the DR) exhibits good agreement with the exact one.

[7]In chapter 2 we only introduced the various energy-independence based omissions slowly, as we went through the derivation, but one could formally immediately discard all energy dependence back in (2.4) to get the same result.

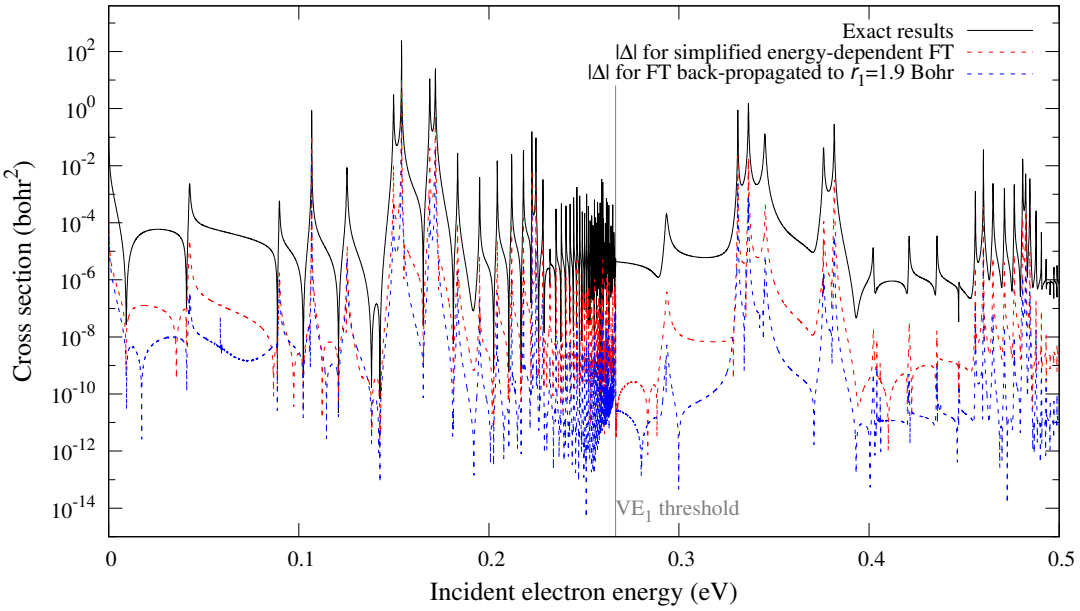

Figure 4.5: Comparison of the DR cross sections for the two backpropagated energy-dependent FT methods. Again, we plot only the exact data (solid black curve) and the absolute values of differences $|\Delta|$ from the exact results (dashed curves). The full backpropagated FT (at $r_1 = 1.9$ bohr) is the blue curve and the simplified backpropagation model is the red curve.

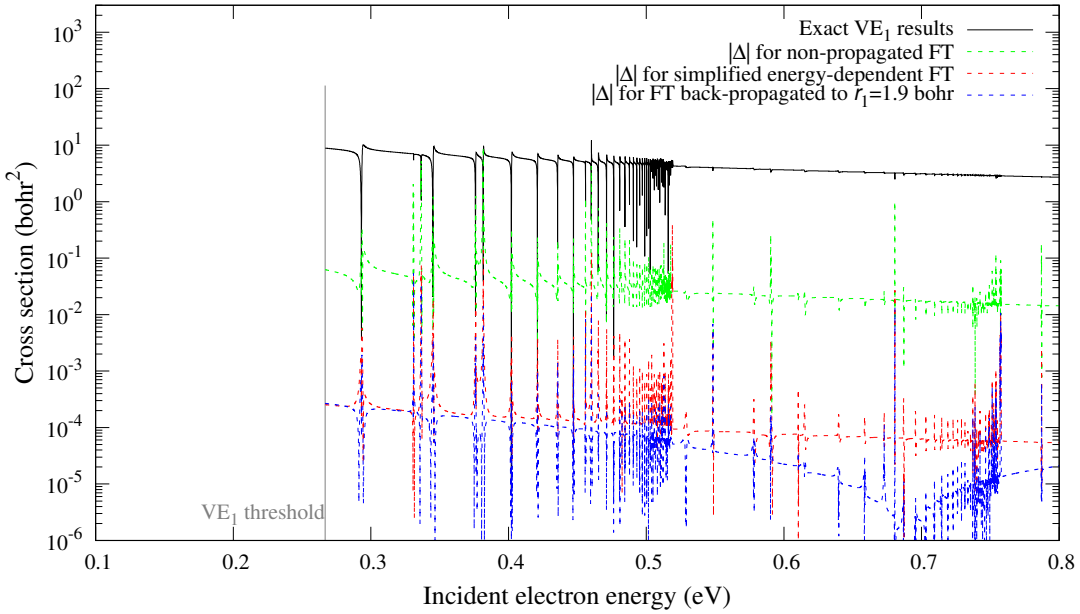

Figure 4.6: Comparison of the inelastic VE cross sections for energy-dependent FT methods. The curves are organised as in Fig. 4.5 with the addition of a green curve representing $|\Delta|$ for non-propagated computation.

5. Comparison with an accurate experiment

The results of the first three studies were rather satisfying in the sense that we achieved good agreement among the multiple theoretical approaches that we implemented and improved. Nonetheless, we were still only in possession of comparisons between theoretical models (and for the simplest symmetry of the simplest molecule at that) and no experimental data. We wished to compare our methods' results with a real measured system and fortunately in that time frame DR rate coefficient data of very high accuracy featuring a simple enough molecule has indeed been published.

5.1 The choice of HeH^+

The HeH^+ ion and its destruction via DR have a strong relevance to cosmological studies. The HeH^+ ion itself is probably the oldest molecule in the universe and yet it has evaded detection by astrophysicists for decades. Recently, it was finally detected in the NGC 7027 nebula by Güsten *et al.* [35]. To analyze their data they created a simple reaction chain model with three main processes:

$$\mathrm{He}^+ + \mathrm{H} \rightarrow \mathrm{HeH}^+ + h\nu \,, \tag{5.1}$$

$$\mathrm{HeH}^+ + e^- \rightarrow \mathrm{He} + \mathrm{H} \,, \tag{5.2}$$

$$\mathrm{HeH}^+ + \mathrm{H} \rightarrow \mathrm{H}_2^+ + \mathrm{He} \,, \tag{5.3}$$

of which the third process (5.3) can be neglected at densities relevant to NGC 7027. They used estimated rate coefficients of the remaining processes to compute the emissivity of the HeH^+ $N^+ = 1 \rightarrow 0$ transition (here N^+ is the molecular rotational quantum number). The model predicted an integrated main beam brightness temperature approximately four times lower than the observed quantity. This implies that either the radiative association (5.1) rate underestimates the production of HeH^+ or the dissociative recombination (5.2) rate overestimates their destruction.

At this point the (also recently) published experimental results [36] from the state-of-the-art Cryogenic Storage Ring (CSR) in Heidelberg enter the picture. These contain highly accurate measurements of rate constants for the DR of cold HeH^+ ions. Our fourth publication [D] thus details the application of the FT method to model the DR of HeH^+ and it compares the computed rates with the experimental results from the CSR. Compared to the publication we use a slightly different notation here to stay consistent throughout the thesis. We still use j to denote the vibrational states as opposed to ν in the publication. The electronic angular momentum quantum number is l (unchanged) and the cation's rotational quantum number is N^+ (changed from j).

5.2 Application of FT to $HeH^+ + e^-$

We apply the simplified version of the energy-dependent FT method described in section 4.4 to the $HeH^+ + e^-$ system. This means that compared to $H_2^+ + e^-$ the main changes are:

- The nuclear Hamiltonian (1.2) now contains a rotational term $\frac{N^+(N^++1)}{2MR^2}$, the Morse potential $V_0(R)$ (1.4) is replaced by the ground-state $^1\Sigma_g^+$ potential curve of HeH^+ from Ref. [37] and the atom-ion reduced mass is now $M = 1467.28$ a.u.

- The body-frame quantum defect $\underline{\mu}^\Lambda(\epsilon, R)$ is now a set of three matrices of $(3-\Lambda)\times(3-\Lambda)$ dimension with Λ being the projection of the Rydberg electron angular momentum l onto the molecular axis (the matrix elements correspond to angular momenta of the colliding electron). The limitation $l_{\max} = 2$ was previously proven sufficient [20] and it is used here.

- The computed DR cross section will now have indices for the initial vibrational state and angular momentum states, that is $\sigma_{j'N^{+\prime}l'}{}^{J'\eta}(E)$. Here $\vec{J'} = \vec{N^{+\prime}} + \vec{l'}$ is the total angular momentum and $\eta(-1)^{J'}$ is the parity of the system. After computing $\sigma_{j'N^{+\prime}l'}{}^{J'\eta}(E)$, the state-dependent cross section is obtained as the following sum

$$\sigma_{j'N^{+\prime}}(E) = \frac{1}{2N^{+\prime}+1}\sum_{\eta J'l'}(2J'+1)\sigma^{J'\eta}_{j'N^{+\prime}l'}(E)\ , \tag{5.4}$$

  and from that the initial-state-dependent DR rate is

$$\alpha_{j'N^{+\prime}}(E) = \sqrt{2(E - E_{j'N^{+\prime}})}\,\sigma_{j'N^{+\prime}}(E)\ . \tag{5.5}$$

The quantum defect matrices were computed using the diatomic UK Molecular R-matrix codes [38][8] with the boundary $r_0 = 20$ bohrs. Bound electrons were described in the Slater-type basis [39] of triple-zeta quality. The energy dependence of matrices $\underline{\mu}^\Lambda(\epsilon, R)$ was linearly approximated

$$\underline{\mu}^\Lambda(R,\epsilon) = \underline{\mu}^\Lambda(R) + \epsilon\underline{\mu'}^\Lambda(R)\ , \tag{5.6}$$

from fixed-nuclei computations at two collision energies: $\epsilon_1 = 20$ meV and $\epsilon_2 = 420$ meV (this was determined to be stable and accurate enough by testing different energy values). The nuclear basis was once again constructed with the ECS technique with the bending point at $R_0 = 10$ bohr, a bending angle of $\theta = 40°$ and the maximum length of the bent contour parametrized by $R_m = 25$ bohr.

To compare our output data with the CSR experiment we first have to convolve it over an electron energy distribution representing the experimental environment. For a storage-ring experiment the electron beam has an anisotropic energy distribution. The electron ion beam parallel velocity spread is small and the dominant divergence is in the perpendicular direction ($\Delta E_{||} = 0.1$ meV and $\Delta E_\perp = 2$ meV in Ref. [36]). A detailed description of the anisotropic and thermal convolutions used can be found in Refs. [13, 15]. Afterwards, one additional

[8] Which means that we do not have or need an explicit model interaction potential $V(R, r)$.

data processing step is needed and that is the toroidal correction [40, 41] which accounts for the collisional events happening in the bending areas of the experimental apparatus where the electronic and ionic beams may have higher relative velocity. Collisional events occurring in these areas increase the energy spread.

Figs. 5.1, 5.2 and 5.3 compare our results for the low-energy DR of $HeH^+ + e^-$ with the CSR experiment (for three different starting values of $N^{+\prime}$). They show our results both with and without the toroidal correction. We try to estimate the uncertainty of our calculations by implementing a random noise matrix $\delta\underline{\mu}^{\Lambda}$ which increased or decreased the original $\underline{\mu}^{\Lambda}(R, \epsilon)$ by up to 0.2% (this value was chosen based on our observations of variations of the quantum defect matrix due to electronic basis choice and extent of the space of configuration interaction). The effect of this is more pronounced at lower energies. There's a variation of 30%-50% in the result at energies below 1 meV and by a factor of up to 3 for the highest peak at around 45 meV (for $N^{+\prime} = 0$), 40 meV ($N^{+\prime} = 1$) and 20 meV ($N^{+\prime} = 2$). As we have shown in chapter 4, using the energy-dependent quantum defects can move closed-channel resonances around quite significantly. For example, a closed-channel resonance previously (in an energy-independent FT treatment [20]) at 1 meV, which dominated the near-zero energy DR rate, now moves to negative collision energies (becoming a bound state) and no longer affects the DR rate, which results in the rate's significant decrease at near-zero energies (compare with Fig. 13 of Ref. [20]). Overall our results show improved agreement with the experiment over previous energy-independent FT studies (especially in the low-energy regions).

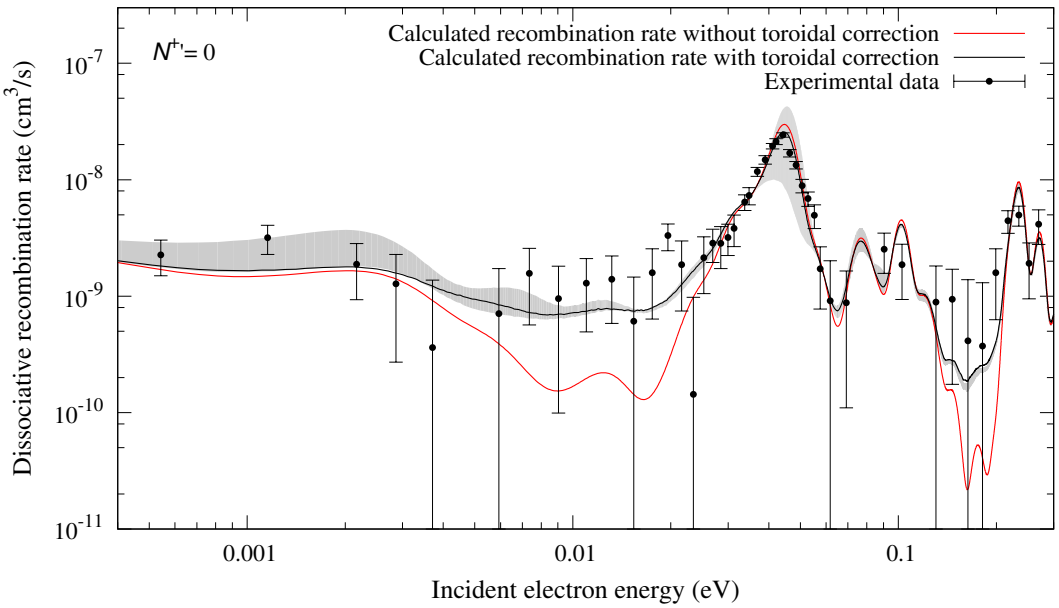

Figure 5.1: Anisotropically averaged (for $\Delta E_{||} = 0.1$ meV and $\Delta E_{\perp} = 2$ meV) DR rate of $HeH^+ + e^-$ with initial vibrational state $j' = 0$ and initial rotational state $N^{+\prime} = 0$. The red curve are our results without the toroidal correction and the black curve includes it. The light grey area is the estimated uncertainty computed using the noise matrix $\delta\underline{\mu}^{\Lambda}$. The data points with error bars are the measured DR rates from the CSR experiment.

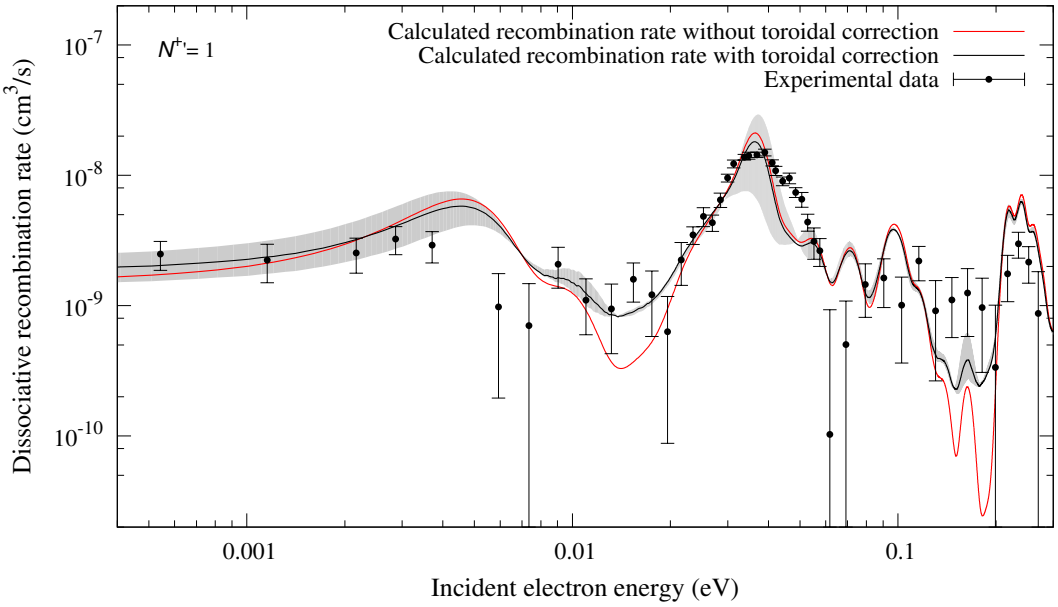

Figure 5.2: Same as Fig. 5.1 but for initial rotational state $N^{+\prime} = 1$.

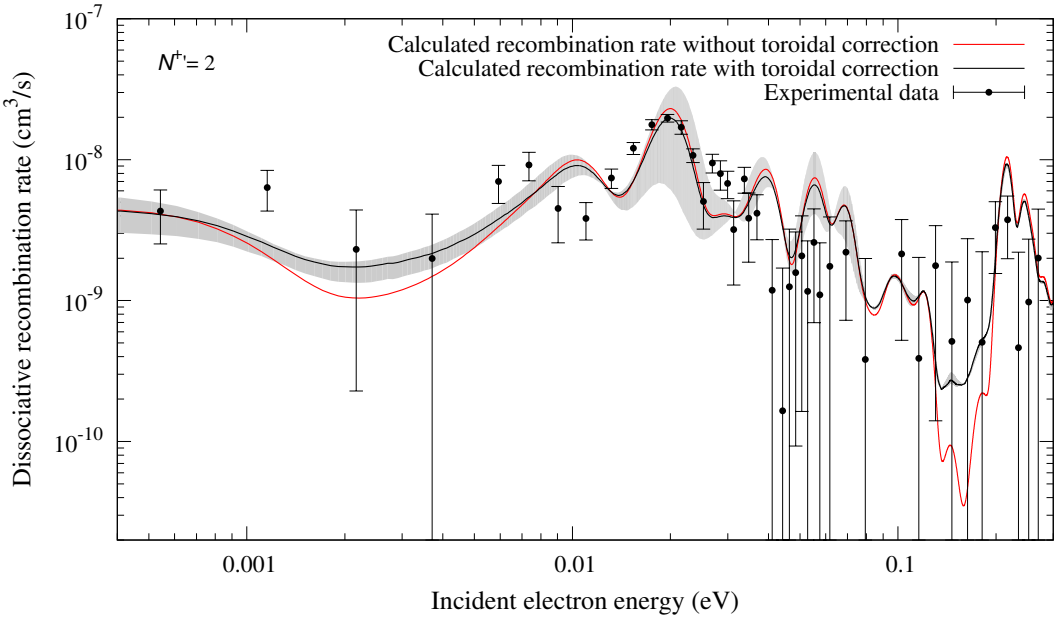

Figure 5.3: Same as Fig. 5.1 but for initial rotational state $N^{+\prime} = 2$.

We also computed plasma rate coefficients by averaging the state specific DR rate over a Maxwellian distribution of colliding electrons. A comparison with plasma rate coefficients computed from the CSR results can be seen in Fig. 5.4 for initial rotational states $N^{+\prime} = 0, 1, 2$. The figure also shows the plasma rate coefficient used for the estimate of the emissivity of the $N^+ = 0 \rightarrow 1$ line of HeH^+ in NGC 7027 [35]. The agreement between our and the CSR plasma rates is overall excellent for $N^{+\prime} = 0$ and quite good for $N^{+\prime} = 1, 2$ at higher temperatures. The lower temperature discrepancies are related to the low energy discrepancies seen in Figs. 5.1, 5.2 and 5.3. Our present estimate of the plasma rate coefficient at 10^4 K (the temperature relevant to the NGC 7027 study) is

slightly above 4.0×10^{-10} cm^3/s, while the plasma rate coefficient used in Ref. [35] was 3.0×10^{-10} cm^3/s. This implies that the astrophysical simulations [35] did not overestimate the rate of destruction of HeH^+ ions through the DR and the high brightness of the $N^+ = 1 \rightarrow 0$ transition in the first HeH^+ detection cannot be attributed to a slower DR process.

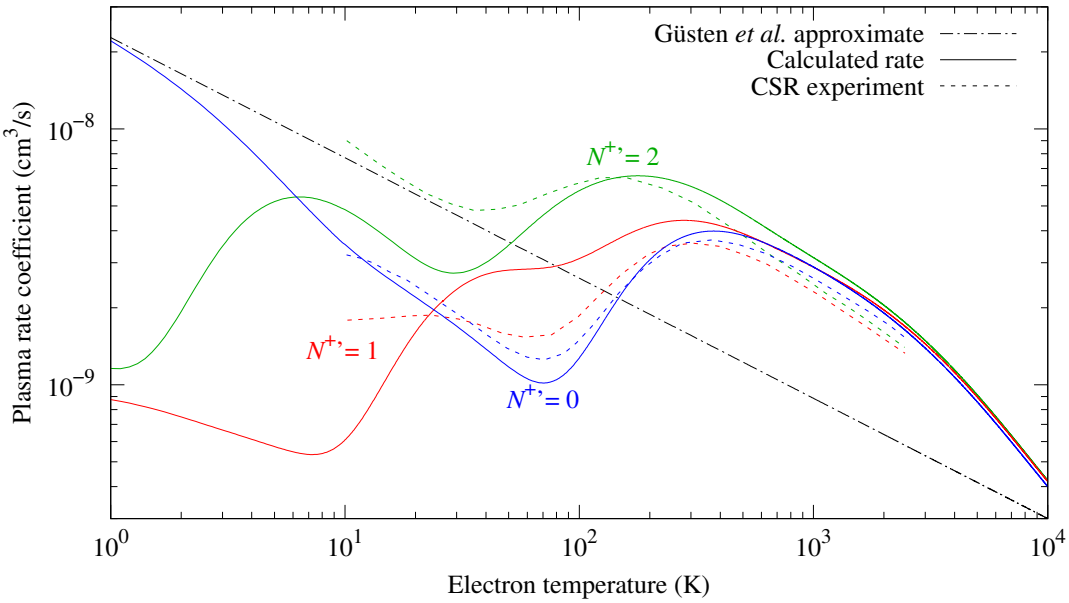

Figure 5.4: Plasma rate coefficients for three initial rotational states $N^{+\prime} = 0, 1, 2$ (blue, red and green curves respectively). The solid curves are our present results, the dashed curves are from the CSR experiment [36] and the black dot-dashed line is the approximation used in the Güsten *et al.* NGC 7027 study [35].

6. Coupled 2D model for the gerade states of H_2

Having tested and improved the various theoretical methods of computing indirect DR for $H_2^+ + e^-$ and even comparing one with the experiment for $HeH^+ + e^-$ we wish to continue to expand the methods to more complicated cases to later describe other real systems. Our next goal is the application of the FT theory to the direct mechanism of the DR. The benchmarking system will be a model of the DR of $H_2^+ + e^-$ in the singlet gerade symmetry. For this we have developed[9] a model electronic-nuclear interaction potential with three angular-momentum channels (including couplings) $V^{ll'}(R,r)$ with $l = 0, 1, 2$ (for the s-, p- and d-channels). The full model Hamiltonian is

$$H^{ll'}(R,r) = \left[H_{\rm n}^{l}(R) + H_{\rm e}^{l}(r)\right]\delta_{ll'} + V^{ll'}(R,r)\ , \tag{6.1}$$

where $\delta_{ll'}$ is the Kronecker delta. The electronic Hamiltonian $H_{\rm e}^{l}(r)$ is again defined by (1.3) and the nuclear Hamiltonian $H_{\rm n}^{l}(R)$ is

$$H_{\rm n}^{l}(R) = -\frac{1}{2M}\frac{\partial^2}{\partial R^2} + V_0^{l}(R)\ . \tag{6.2}$$

The nuclear potentials $V_0^l(R)$ are now the target potentials for the singlet gerade states of $H_2^+ + e^-$, with the Rydberg electron having the angular momentum l. The the potentials are equal for the s and d partial waves, i.e. $V_0^0(R) = V_0^2(R)$. The potentials we use can be found in Madsen's and Peek's work [42]. The potential $V^{ll'}(R,r)$ is comprised of three diagonal interaction terms V^{00}, V^{11}, V^{22} and two off-diagonal coupling terms V^{01}, V^{12}. The direct coupling of the s- and d-channels (V^{02}) is neglected. All the interaction terms share the form

$$V^{ll'}(R,r) = \lambda^{ll'}(R)e^{-r^2/\omega^2}\ , \tag{6.3}$$

and for all the potentials $\omega = 2$ bohrs. For the diagonal interaction potentials, the nuclear part is chosen as a sum of two Gaussian curves

$$\lambda^{ll}(R) = \alpha_1^{ll} e^{-\left(\frac{R-\alpha_2^{ll}}{\alpha_3^{ll}}\right)^2} + \alpha_4^{ll} e^{-\left(\frac{R-\alpha_5^{ll}}{\alpha_6^{ll}}\right)^2}\ . \tag{6.4}$$

The first coupling potential $V^{01}(R,r)$ contains a "quartic exponential"

$$\lambda^{01}(R) = \alpha_1^{01} e^{-\left(\frac{R-\alpha_2^{01}}{\alpha_3^{01}}\right)^4}\ , \tag{6.5}$$

and the second coupling potential V^{12} contains a single Gaussian

$$\lambda^{12}(R) = \alpha_1^{12} e^{-\left(\frac{R-\alpha_2^{12}}{\alpha_3^{12}}\right)^2}\ . \tag{6.6}$$

[9] It might be more prudent to say "are developing" since the model is still subject to change.

The Table 6.1 contains all the necessary coefficients. As noted in the introduction, the input distances are measured in bohrs and the output potential energy is in hartrees. For a visual representation, Fig. 6.1 shows the R-dependence of all the parts of $\lambda^{ll'}(R) = V^{ll'}(R, r = 0)$ (the electronic coordinate dependence is the same Gaussian scaling $e^{\frac{-r^2}{4\text{bohr}^2}}$ in all cases).

	$\alpha_1^{ll'}$	$\alpha_2^{ll'}$	$\alpha_3^{ll'}$	$\alpha_4^{ll'}$	$\alpha_5^{ll'}$	$\alpha_6^{ll'}$
V^{00}	0.350802	4.53741	2.10017	0.168061	2.71464	1.17950
V^{11}	-0.744042	2.89011	3.05122	-0.327764	7.33829	3.40565
V^{22}	-1.13912	8.50097	7.04271	-1.61629	21.1034	14.3257
V^{01}	-0.1960	0	5.52884	-	-	-
V^{12}	-0.4	2.8	4.0	-	-	-

Table 6.1: Table of coefficients for potential modeling the singlet gerade case.

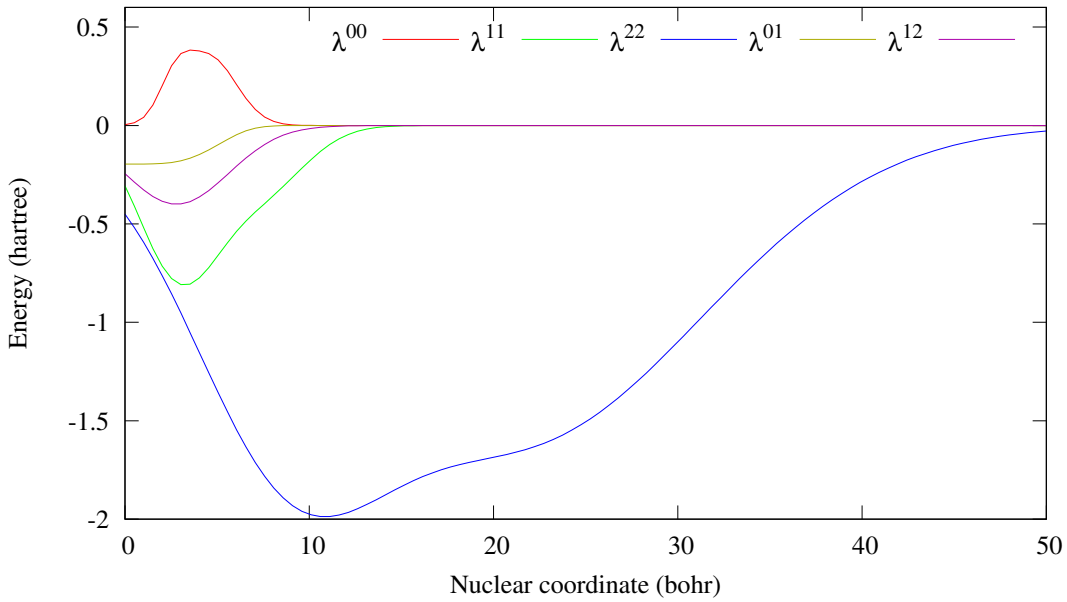

Figure 6.1: The nuclear coordinate dependence of our model interaction potential for $H_2^+ + e^-$ in the singlet gerade symmetry.

The presented form of the coupling interaction potential $V^{ll'}(R, r)$ is a result of the search for a model potential that reproduces the adiabatic potential curves of excited $^1\Sigma_g^+$ states of the hydrogen molecule, namely the well known EF, GK and $H\bar{H}$ curves [43]. We compute such curves by solving the l-coupled Schrödinger equation

$$\left[H_e^l(r) + V_0^l(R) - E_k^{\text{adi}}(R)\right] \psi_k^l(r; R) = -\sum_{l'=0,1,2} V^{ll'}(R, r)\psi_k^{l'}(r; R) \ , \quad \text{for a fixed } R \ . \tag{6.7}$$

Solving (6.7) with the boundary condition $\psi_k^{l'}(r = r_0; R) = 0$ (for a large enough r_0, for all l') and connecting the energies $E_k^{\text{adi}}(R)$ over a range of R-values gives us the adiabatic potential curves. These curves are shown in Fig. 6.2 which

compares them to the EF, GK and $H\bar{H}$ curves of L. Wolniewicz and K. Dressler [44, 43] (the figure also shows parts of the O and P curves though the model was not tailored to reproduce them). The curves $V_0^l(R)$ of Madsen and Peek [42] are also included for more clarity.

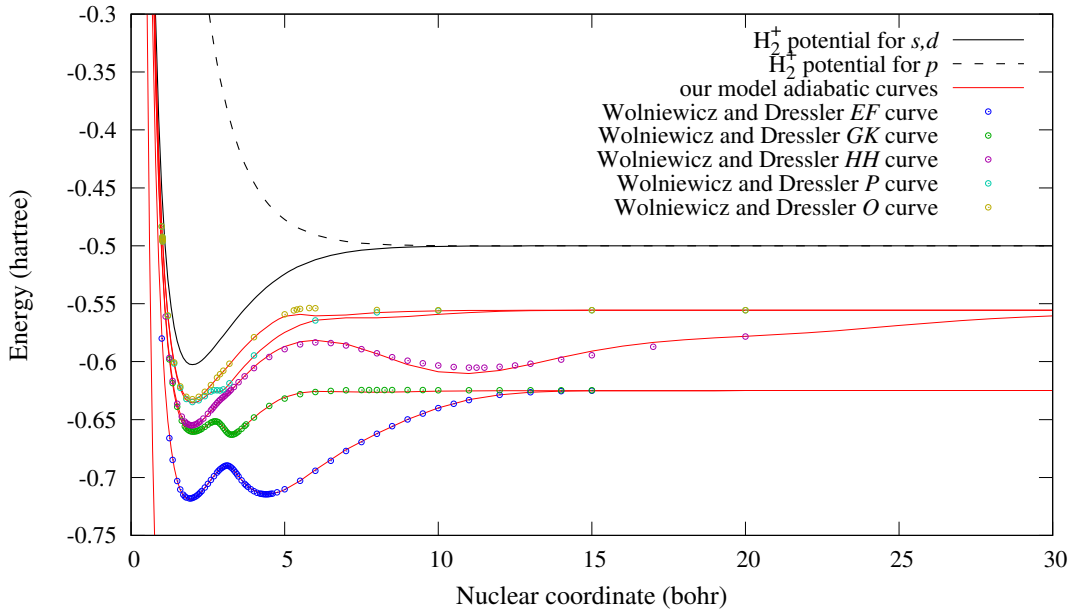

Figure 6.2: Comparison of the lowest second through sixth adiabatic potential curves computed with our model potential (red curves) and those of Wolniewicz and Dressler (points). The black curves show the $V_0^l(R)$ of Madsen and Peek [42]. Part of the bottom adiabatic curve is also shown but it quickly falls below the range of the graph.

It is important to note here that $V^{ll'}(R, r)$ is not refined as the accurate model potential for the singlet gerade hydrogen states. It is merely a tool that we plan to use to compare our DR computational methods once we implement the 2D R-matrix approach and the energy dependent FT approach (which will now be a *ro*vibrational frame transformation) for three coupled rotational channels. As such, we deem the discrepancies visible in Fig. 6.2 between our and previous results as acceptable even though adiabatic potential curves for hydrogen are typically known with a much higher degree of accuracy. Interestingly, the model was not at all tailored to reproduce the O and P curves, yet it does so decently in the reaction zone. On the other hand (and not directly shown in the image), the lowest adiabatic curve computed exhibits unphysical behavior at distances of 2 - 10 bohr. Similarly to the model interaction potential from Hamilton's thesis [10] used for the ungerade case, we believe that the bottom unphysical curve will have a negligible impact on the overall DR results (compare orders of magnitude in Figures 3.1 and 3.2 or Fig. 4 of [A]). Looking back to Fig. 6.1, we can see that the long-range character of the $V^{22}(R, r = 0)$ term is responsible for the reproduction of the wide second minimum of the $H\bar{H}$ curve. Physically speaking, the minimum should be related to the ion-pair curve and not generated so "synthetically". Ultimately, the main strength of this model is its analytical simplicity (mostly the sum and multiplication of just a few Gaussian functions) which makes it easy to insert into any method.

6.1 Properties of the model

The aim of this section is to present three selected physical properties of the model and to compare them with the known data. Although, as mentioned above, the model Hamiltonian does not aim for an accurate reproduction of the molecular hydrogen in the singlet gerade symmetry, it is still desired to have it reasonably close to a real physical system. The quantities we will focus on are the vibronic energies, the adiabatic resonance positions and widths, and the adiabatic quantum defects.

6.1.1 Vibronic energies

The adiabatic potential curves of Fig. 6.2 can be used to obtain the BOA vibronic energies by solving a one-dimensional nuclear Schrödinger equation with the curves EF, GK, $H\bar{H}$ used in place of the nuclear potential and with a bound state boundary condition, so we solve (assuming rotational state $N = 0$)

$$\left[-\frac{1}{2M}\frac{\partial^2}{\partial R^2} + E_k^{\mathrm{adi}}(R)\right]\phi_{km}(R) = E_{km}^{\mathrm{vib}}\phi_{km}(R)\ , \qquad \text{for } \phi_{km}(R_0) = 0\ , \tag{6.8}$$

for some large R_0, where the k index corresponds to the EF, GK and $H\bar{H}$ curves. Additionally, during the computation of the adiabatic curves (6.7) we can easily calculate the diagonal correction terms

$$V_k^{\mathrm{corr}}(R) = \sum_{l=0,1,2}\frac{1}{2M}\left\langle \frac{\partial}{\partial R}\psi_k^l(r;R)\middle|\frac{\partial}{\partial R}\psi_k^l(r;R)\right\rangle_r\ , \tag{6.9}$$

where k is again chosen to correspond to the studied adiabatic curves and $\langle\ .\ |\ .\ \rangle_r$ is integration only over the electronic coordinate. Adding these $V_k^{\mathrm{corr}}(R)$ terms to the energies $E_k^{\mathrm{adi}}(R)$ in the lhs of (6.9) is the second-order BOA correction. We can then compare the vibronic energies E_{km}^{vib} with experimental results as was done by Jungen and Ross [45] for the real molecular hydrogen. This is shown in Table 6.2 where the third column contains the experimental data of Ref. [45] minus our BOA vibronic energy values (the units are now wave numbers (cm^{-1}) for an easier comparison with the reference). We do not expect to get nearly the same amount of accuracy as Ross and Jungen with their MQDT method but it is once again reassuring to see that our results generally hold a similar level of accuracy as the BOA results in the cited work (our root mean square error is about 118 cm^{-1}, theirs was about 110 cm^{-1}). Looking more closely at the results there is a trend of GK and $H\bar{H}$ vibronic states being below the experimental results while EF states are both above and below their expected values.

Vibronic state	Vibronic energy (cm^{-1})	Comparison to Ref. [45] (cm^{-1})	Vibronic state	Vibronic energy (cm^{-1})	Comparison to Ref. [45] (cm^{-1})
E0	98949.68	215.10	GK1	111546.31	266.36
F0	99328.61	35.31	EF19	112176.81	-70.72
F1	100500.70	58.23	H0	112782.32	175.25
E1	101366.27	128.48	EF20	112794.93	-83.13
F2	101642.30	56.63	GK2	113129.73	128.51
F3	102735.15	43.13	EF21	113397.40	-3.90
E3	103485.05	74.54	GK3	113822.54	222.12
F4	103820.07	18.47	EF22	113982.87	-121.47
F5	104719.16	11.45	EF23	114550.44	-39.90
EF9	105387.11	-2.21	GK4	115032.05	67.79
EF10	106011.85	-45.69	H1	115052.05	199.47
EF11	106768.25	-55.18	EF24	115098.71	-73.87
EF12	107495.45	-69.58	EF25	115625.20	-61.50
EF13	108186.65	-88.09	GK5	116025.12	139.69
EF14	108881.12	-87.57	EF26	116126.64	-85.05
EF15	109573.13	-79.23	EF27	116598.97	-90.73
EF16	110247.41	-84.03	GK6	116984.65	96.78
EF17	110903.03	-108.84	EF28	117037.32	-121.96
GK0	111381.77	247.04	H2	117180.12	116.91

Table 6.2: EF, GK and $H\bar{H}$ curve vibronic energies. The first column identifies the state, the second column contains the energies relative to the $N = 0, m = 0$ level of $\tilde{X}\ ^1\Sigma_g^+$ ground state and the third column is the difference between our result and the observed value of Ref. [45] (observed - calculated).

6.1.2 Adiabatic $^1\Sigma_g^+$ resonance

Another physical test that we can subject our model to is a resonance search akin to Ref. [46]. We first expand the Eq. (6.7) with an electronic Bloch operator (and re-label $E_k^{\rm adi}(R) = E_k(R)$) to get

$$\left[H_{\rm e}^l(r) + V_0^l(R) - E_k(R) + \frac{1}{2}\delta(r - r_0)\frac{\partial}{\partial r}\right]\psi_k^l(r;R) = -\sum_{l'=0,1,2} V^{ll'}(R,r)\psi_k^{l'}(r;R)\ , \quad \text{for a fixed } R\ . \tag{6.10}$$

If we solve this without imposing the zero-boundary condition at r_0, we can then compute a short-range fixed-nuclei 3×3 R matrix via

$$R^{ll'}(E,R) = \frac{1}{2}\sum_k \frac{\psi_k^l(r = r_0;R)\,\psi_k^{l'}(r = r_0;R)}{E_k(R) - E}\ , \tag{6.11}$$

for some given total energy E. We can transform this R matrix into the short-range K matrix just like we did in section 3.1 (though the matrices are now indexed by l)

$$\underline{K} = \left(\underline{f} - \underline{f}'\underline{R}\right)\left(\underline{g} - \underline{g}'\underline{R}\right)^{-1}\ , \tag{6.12}$$

where $\underline{f}$, $\underline{g}$, $\underline{f}'$ and $\underline{g}'$ are now diagonal matrices of Coulomb functions indexed by the quantum number l evaluated at $r = r_0$[10] and momentum $k^l = \sqrt{E - V_0^l(R)}$. The short-range matrix $K^{ll'}(E,R)$ is computed for total energies above the s- and d- H_2^+ potential curve $V_0^{l=0}(R)$ and below the repulsive p-curve $V_0^{l=1}(R)$. This gives us two open channels (s and d) and one closed p-channel. The channel elimination into the open-channel $\underline{R}^{\text{phys}}$ matrix is simply

$$K^{ll',\text{phys}} = K^{ll'} - K^{l\,1}\left[K^{1\,1} + \tan\left(\frac{\pi}{\sqrt{2(V_0^1(R) - E)}}\right)\right]^{-1} K^{1\,l'}\,, \qquad \text{for } l, l' \in \{0, 2\}\,. \tag{6.13}$$

Here we omitted (E,R) after each instance of $K^{ll'}$ for the sake of brevity. The eigenvalues of this new 2×2 $\underline{K}^{\text{phys}}$ matrix are $\tan(\delta^i(E,R))$ and we call $\delta^i(E,R)$ the physical eigenphase shifts. Sampling these eigenphase shifts at a selected nuclear R for a dense series of energies above the $V_0^0(R)$ curve results in ascending curves like those shown in Fig. 6.3. The step-like structures in the sum of these curves show the positions of resonances. The data can be compared with the work of Greene and Yoo [46] along with the resonance widths obtained from the energy derivative of $\delta^i(E,R)$. The table 6.3 shows the comparison for select values of R.

It is clear that the present model does not only reproduce the existence of the resonance but it also places it reasonably close to the previously computed ab initio values. Our model results have a tendency to be slightly higher in energy, though for 2.6 bohr the studied lowest resonance curve has just passed under the $V_0^0(R)$ potential curve (hence the empty entry in the table) in our case while in Ref. [46] it is still closely above. The resonance widths Γ_r in our model tend to be larger (up to two times).

R (bohr)	E_r (model)	Γ_r (model)	E_r (Greene, Yoo)	Γ_r (Greene, Yoo)
1.0	0.25171	0.028	0.23726	0.0229
1.2	0.05753	0.035	0.04158	0.0241
1.4	−0.09948	0.043	−0.10799	0.0251
1.6	−0.22494	0.052	−0.22886	0.0259
1.8	−0.32475	0.059	−0.32768	0.0265
2.0	−0.40663	0.068	−0.40912	0.0288
2.2	−0.47684	0.077	−0.47731	0.0335
2.6	-	-	−0.57388	0.0525

Table 6.3: Positions E_r and widths Γ_r of the lowest $^1\Sigma_g$ resonance in H_2 for our model compared with Ref. [46]. Results are given in hartrees.

[10]When working with closed-channel asymptotic solutions, r_0 has to be chosen carefully. It has to be large enough to encompass the model interaction potential but also not too large, so that the f, g functions in closed-channels do not diverge too much (potentially causing loss of accuracy in (6.12)). In our case $r_0 = 8$ bohr proved to be sufficient for this test. On the other hand, during the computation of the adiabatic curves we can extend r_0 much farther to describe the higher curves well.

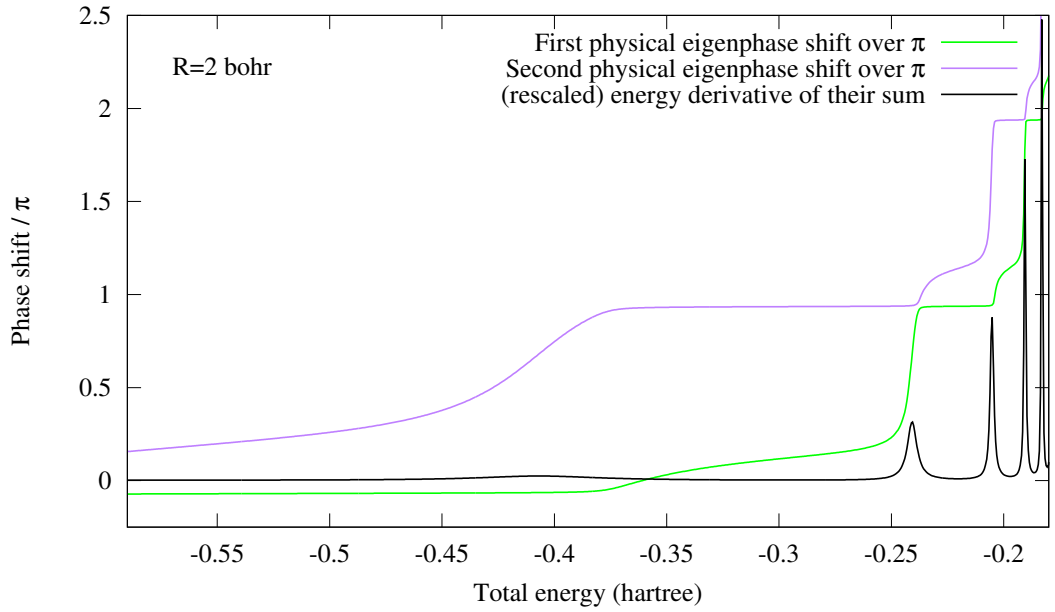

Figure 6.3: The two eigenphase shifts (green and cyan curves) in the energy window between $V_0^{l=0}(R)$ and $V_0^{l=1}(R)$ and the energy derivative of their sum (black curve) which has been divided by a constant factor of 400 to fit into the image. The steps in the shifts as well as peaks in the derivative show resonance positions. Computed at $R = 2$ bohr.

6.1.3 Adiabatic quantum defect matrix

In the last simple test the computed quantum defect matrix is compared with the same data reported for the real molecular system previously [47]. At this

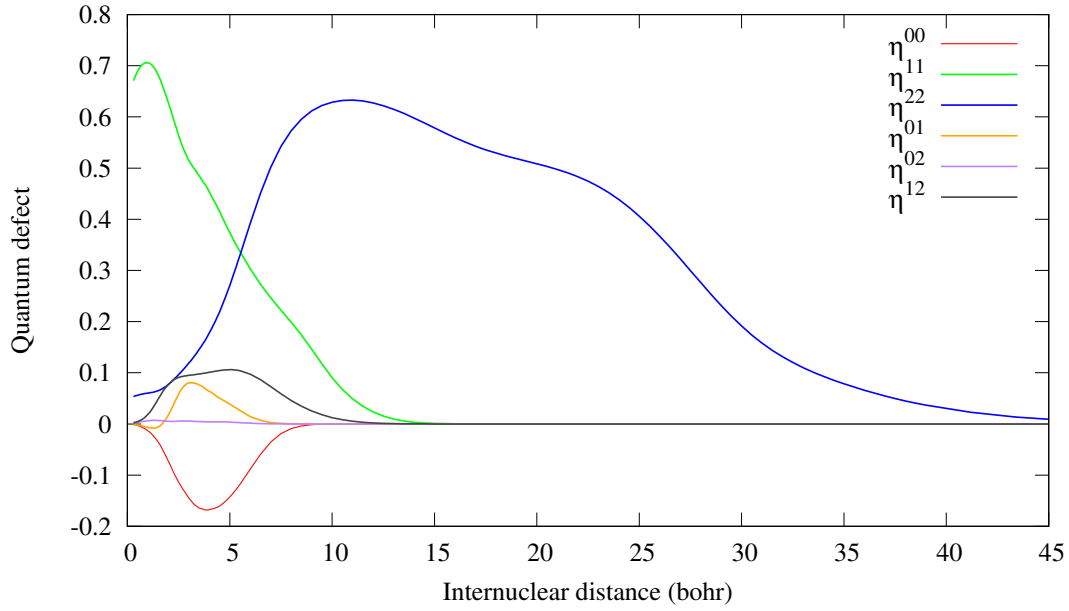

Figure 6.4: R-dependence of the full quantum defect matrix at $E = V_0^0(R)$.

point, to coincide with the reference, we start to use a slightly different pair of Coulomb functions when compared with the previous chapters. We can denote

them $\{f^0, g^0\}$ and this pair is now equal to the pair $\{f, -h\}$ from Seaton's work [5, 23]. The difference from the previous pair is that the new one has different energy normalization but behaves better at negative energies. The quantum defect computed against this new pair will be denoted η instead of μ. The steps to get the adiabatic quantum defect matrix are now straightforward. At first, we follow the same procedure as for the resonance search: we solve (6.10) without a boundary condition at r_0 and compute the 3×3 R matrix (6.11). Then the short-range K matrix is computed from (6.12) but the pair $\{f, g\}$ is replaced by the $\{f^0, g^0\}$ pair. Let us denote this altered reaction matrix as $\underline{K^0}$. The closed channels will not be eliminated, the short-range $\underline{\eta}$ matrix can be defined in open and closed channels. We simply diagonalize the $\underline{K^0}$-matrix

$$K^{0\,ll'} = \sum_{i=0,1,2} U^{li} \tan(\pi\tau^i) U^{\dagger\, il'} \ . \tag{6.14}$$

Knowing the eigenvalues[11] and eigenvectors the quantum defect matrix $\eta^{ll'}$ can be reconstructed as follows

$$\eta^{ll'} = \sum_{i=0,1,2} U^{li} \tau^i U^{\dagger\, il'} \ . \tag{6.15}$$

Fig. 6.4 shows the full η-defect matrix computed this way for $R = 0$ to 45

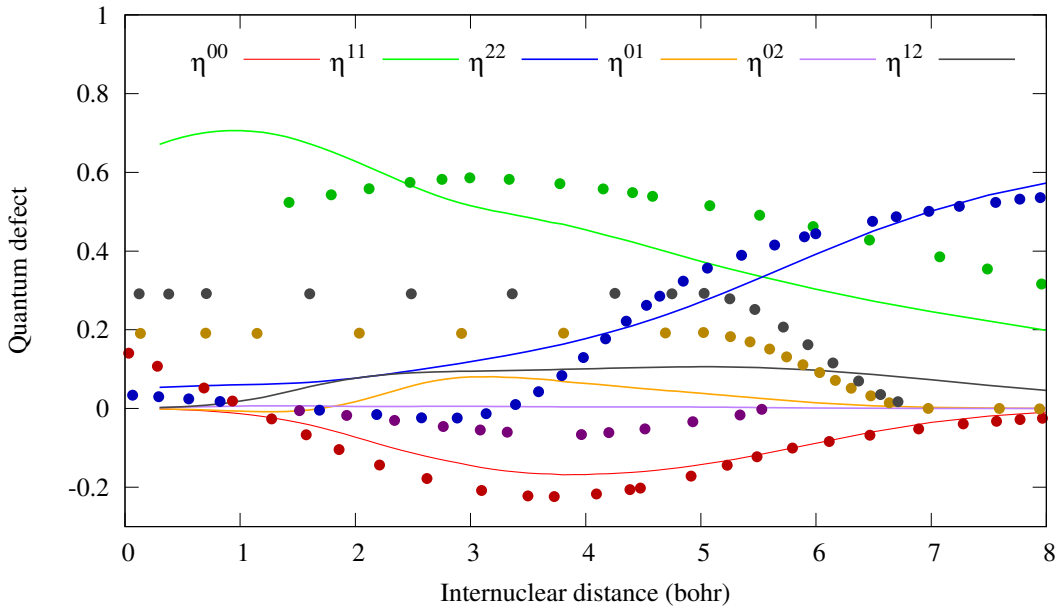

Figure 6.5: Detailed zoom of Fig. 6.4 (full lines) compared with the data extracted form the work of Jungen and Ross [47] (points).

bohr. The symmetrized electronic Schrödinger equation (6.10) was solved on a grid up to $r_0 = 8$ bohrs, with the total energy in (6.11) set equal to the bottom H_2^+ curve $V_0^0(R)$. Fig. 6.5 compares the matrix $\eta^{ll'}(E, R)$ (with $E = V_0^0(R)$) to data extracted from Ref. [47]. It is apparent that the extracted data bear

[11] To obtain a smooth $\tau^{l''}(E, R)$ one must of course keep in mind all the caveats of using the arctangent function to reconstruct a continuous quantity that is not bound to a π-length interval.

a qualitative resemblance to our results but there is no quantitative agreement. However, there are two important points about the data from Ref. [47] that need to be mentioned here. Firstly, their coupling terms η^{01}, η^{12} were arbitrarily set to a constant value and then smoothly matched to zero between 5 and 7 bohr. Secondly, the elements $\eta^{ll'}$ were defined differently in Ref. [47], as they have been related to the elements of the K matrix as follows:

$$K^{ll'} = \tan(\pi\eta^{ll'}) \,, \tag{6.16}$$

instead of (6.14) and (6.15).

6.2 Direct DR of $H_2^+ + e^-$ (singlet gerade channel)

What follows are the yet unpublished results of our current project in which the (full) two-dimensional R-matrix approach of chapter 3 is applied to our gerade model potential. The implementation is similar to the ungerade case with a few additions. The Schrödinger equation (3.1) is expanded into three angular channels

$$\left[H_{\mathrm{n}}^{l}(X) + H_{\mathrm{e}}^{l}(r) - E\right]\psi^{l}(X,r) = -\sum_{l'=0,1,2} V^{ll'}\left(\frac{X}{\sqrt{M}}, r\right)\psi^{l'}(X,r) \,, \tag{6.17}$$

where

$$H_{\mathrm{n}}^{l}(X) = -\frac{1}{2}\frac{\partial^2}{\partial X^2} + V_0^l\left(\frac{X}{\sqrt{M}}\right) \,, \tag{6.18}$$

and $H_{\mathrm{e}}^{l}(r)$ remains the same as in Eq. (1.3). Overall, all the Hamiltonians, potentials and the wave functions now have an added l-indexing.

6.2.1 Construction of the surface channel functions

The physically motivated channel functions on the surfaces $\mathcal{S}_{\mathrm{e}}$ and $\mathcal{S}_{\mathrm{n}}$ (see Fig. 6.6) are now

$$H_{\mathrm{n}}^{l}(X)\phi_{j_{\mathrm{e}}}^{l}(X) = E_{j_{\mathrm{e}}}\phi_{j_{\mathrm{e}}}^{l}(X) \,, \tag{6.19}$$

$$\left[H_{\mathrm{e}}^{l}(r) - E_{j_{\mathrm{n}}}\right]\rho_{j_{\mathrm{n}}}^{l}(r) = -\sum_{l'=0,1,2} V^{ll'}(X_0, r)\rho_{j_{\mathrm{n}}}^{l'}(r) \,. \tag{6.20}$$

The boundary conditions $\phi_{j_{\mathrm{e}}}^{l}(X_0) = 0$ and $\rho_{j_{\mathrm{n}}}^{l}(r_0) = 0$ are again imposed for the respective channel functions. Note that since $V_0^l(R_0) \sim 0$ the $E_{j_{\mathrm{n}}}$ here are identical to the adiabatic $E_k^{\mathrm{adi}}(R_0)$.

We now need to make the semantic distinction: an *eigenfunction* is a single $\phi_{j_{\mathrm{e}}}^{l}(X)$ or $\rho_{j_{\mathrm{n}}}^{l}(r)$ while a *solution* is a vector $\boldsymbol{\phi}_{j_{\mathrm{e}}} = \{\phi_{j_{\mathrm{e}}}^{0}, \phi_{j_{\mathrm{e}}}^{1}, \phi_{j_{\mathrm{e}}}^{2}\}$ or $\boldsymbol{\rho}_{j_{\mathrm{n}}} = \{\rho_{j_{\mathrm{n}}}^{0}, \rho_{j_{\mathrm{n}}}^{1}, \rho_{j_{\mathrm{n}}}^{2}\}$. Assembling the fragmentation channel basis is somewhat more complicated now. The situation is simpler for the coupled part (6.20) where the choice of j_{n} immediately informs the behavior of $\rho_{j_{\mathrm{n}}}^{l}(r)$ for all l and so the solution

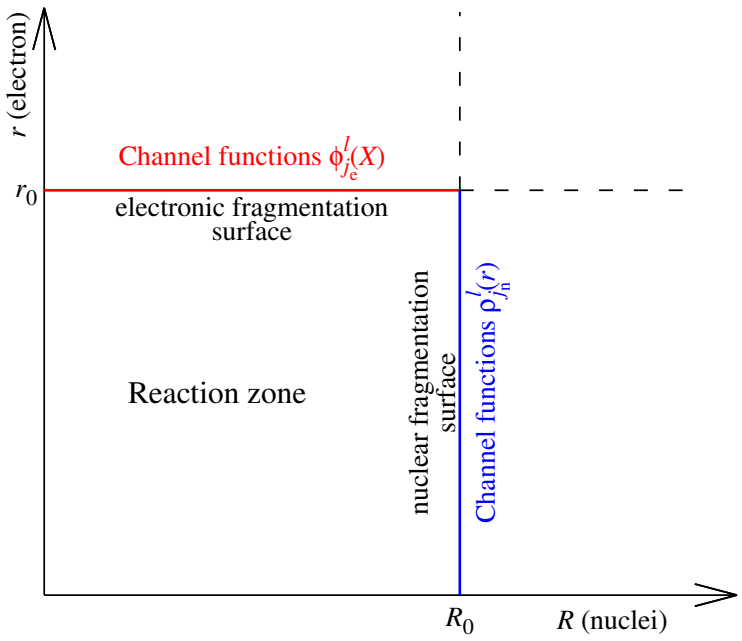

Figure 6.6: Configuration space partitioning and surface channel functions.

$\boldsymbol{\rho}_{j_\mathrm{n}}$ is uniquely defined. For (6.19), picking a j_e that corresponds to an eigenenergy E_{j_e} of $H^l_\mathrm{n}(X)$ usually means that $\phi^{l'}_{j_\mathrm{e}}(X)$ has to be a trivial zero for $l' \neq l$. That is unless H^l_n and $H^{l'}_\mathrm{n}$ share the same eigenenergy. In that case we get two solutions[12] that contain an arbitrary orthonormal combination of the corresponding eigenfunctions[13]. In our case, this will happen for *all* the eigenenergies of H^0_n and H^2_n (identical s and d nuclear potential). The physically motivated choice of channels is such that for each j_e only one part of the solution is non-trivial. We can now unite the two index sets $j = \{j_\mathrm{e}, j_\mathrm{n}\}$ and assemble the fragmentation channel basis $|\boldsymbol{j})$ on the entire surface $\mathcal{S}$

$$j \in j_\mathrm{e}: \ |\boldsymbol{j}) = |\boldsymbol{\phi}_{j_\mathrm{e}}) \text{ on } \mathcal{S}_\mathrm{e} \text{ and } |\boldsymbol{j}) = 0 \text{ on } \mathcal{S}_\mathrm{n} \ , \tag{6.21}$$

$$j \in j_\mathrm{n}: \ |\boldsymbol{j}) = |\boldsymbol{\rho}_{j_\mathrm{n}}) \text{ on } \mathcal{S}_\mathrm{n} \text{ and } |\boldsymbol{j}) = 0 \text{ on } \mathcal{S}_\mathrm{e} \ . \tag{6.22}$$

The symmetrized version of the Hamiltonian (6.1) together with the substitution $R \to X/\sqrt{M}$ reads as

$$\bar{H}^{ll'}(X,r) = H^{ll'}(X,r) + \frac{1}{2}\left[\delta(X-X_0)\frac{\partial}{\partial X} + \delta(r-r_0)\frac{\partial}{\partial r}\right]\delta_{ll'} \ , \tag{6.23}$$

$$H^{ll'} = \left[H^l_\mathrm{n}(X) + H^l_\mathrm{e}(r)\right]\delta_{ll'} + V^{ll'}\left(\frac{X}{\sqrt{M}}, r\right) \ . \tag{6.24}$$

[12]Three solutions if all the three nuclear Hamiltonians share that eigenvalue.

[13]Orthonormal in the sense that if we have two normalized non-trivial eigenfunctions $\phi^0_\mathrm{A}, \phi^2_\mathrm{B}$ solving their respective parts of (6.19) with an identical energy, then we get solutions $\boldsymbol{\phi}_{j_\mathrm{e}} = \{a_1\phi^0_\mathrm{A}, 0, b_1\phi^2_\mathrm{B}\}$ and $\boldsymbol{\phi}_{j'_\mathrm{e}} = \{a_2\phi^0_\mathrm{A}, 0, b_2\phi^2_\mathrm{B}\}$ satisfying $E_{j_\mathrm{e}} = E_{j'_\mathrm{e}}$ and $a_1a_2 + b_1b_2 = 0$, $a_1^2 + b_1^2 = 1 = a_2^2 + b_2^2$. An equivalent applies for three identical eigenvalues, three eigenfunctions and three solutions.

All that is left before we define an R matrix is an analogue of (3.16), which will now be a matrix equation

$$\underline{\bar{H}}|\boldsymbol{\psi}_p\rangle = E_p|\boldsymbol{\psi}_p\rangle \ . \tag{6.25}$$

The Wigner-Eisenbud expansion of the R matrix is then

$$R_{jj'} = \frac{1}{2}\sum_p \frac{(\boldsymbol{j}|\boldsymbol{\psi}_p)\,(\boldsymbol{\psi}_p|\boldsymbol{j}')}{E_p - E} \ , \tag{6.26}$$

with the surface channel states $|\boldsymbol{j})$ defined by Eqs. (6.21) and (6.22) and the terms $(\boldsymbol{j}|\boldsymbol{\psi}_p)$ are now not only surface integrals but also projections over the three vector elements.

6.2.2 Matching to asymptotic functions

The presence of the long-range (see Fig. 6.1) $V^{22}(R,r)$ term in the full Hamiltonian means that to satisfy the asymptotic behavior (1.7) with a sufficient degree of accuracy, we would require a very large nuclear box size R_0 which results in a very long computation time when solving (6.25). Fortunately, this problem can be circumvented. Since the range of the off-diagonal coupling terms of the potential is much shorter, it is possible to shrink the 2D computational box in such a way that they still satisfy (1.7), while the missing part of the interaction diagonal terms V^{ll} will be included in a different way. Using a smaller 2D box we will still follow the steps up to (6.26). The non-constant nature of the interaction potential beyond R_0 simply means that we can no longer just use Bessel functions for the outer-region solutions in nuclear fragmentation channels. Instead, we have to use functions that are the outgoing- and incoming-nuclear-wave solutions on potentials corresponding to the adiabatic curves of Fig. 6.2. In other words, whenever we solve (6.20) on the surface $\mathcal{S}_\mathrm{n}$ we pair the solution $\boldsymbol{\rho}_{j_\mathrm{n}}(r)$ to one of the adiabatic curves (the channel energy E_{j_n} is equal to the value of one of these curves at $R = R_0$). The matching nuclear functions form the diagonal matrices $\underline{\mathcal{F}}, \underline{\mathcal{G}}$ for some given total energy E. Instead of using the original $F^0_{j_\mathrm{n}}(X), G^0_{j_\mathrm{n}}(X)$ from Eqs. (3.17)-(3.20), we need to find solutions of

$$\left[\frac{\partial^2}{\partial R^2} + 2M\left(E - E^{\mathrm{adi}}_{j_\mathrm{n}}(R)\right)\right] y_{j_\mathrm{n}}(R,E) = 0 \ , \ \text{for } R \geq R_0 \ . \tag{6.27}$$

For this we employ the Milne phase amplitude method described by Greene, Rau and Fano in Ref. [48] in section IV. B. It is known that all the independent solutions to (6.27) can be expressed through any particular solution of

$$\left[\frac{\partial^2}{\partial R^2} + 2M\left(E - E^{\mathrm{adi}}_{j_\mathrm{n}}(R)\right)\right] \alpha_{j_\mathrm{n}}(R,E) = \frac{1}{\alpha^3_{j_\mathrm{n}}(R,E)} \ . \tag{6.28}$$

With the introduction of[14]

$$\theta_{j_\mathrm{n}}(R,E) = \int^R \alpha^{-2}_{j_\mathrm{n}}(R',E)dR' \ , \tag{6.29}$$

[14]Other works usually denote this phase ϕ but we use θ to avoid confusion with nuclear wave functions.

the general solution $y_{j_n}(R,E)$ can be expressed as

$$y_{j_n}(R,E) = a\alpha_{j_n}(R,E)\sin\left(\int^R \alpha_{j_n}^{-2}(R',E)dR' + b\right) \ , \tag{6.30}$$

with arbitrary constants a and b. Note also the arbitrarity within α_{j_n} since it can be any solution of (6.28). Following Ref. [48] we use the boundary condition $\alpha_{j_n}(R_0,E) = \sqrt{2M(E-E_{j_n}^{\rm adi}(R_0))}$. Thus, instead of $F_{j_n}^0(X), G_{j_n}^0(X)$ we will simply use the new pair

$$\tilde{F}_{j_n}(X) = \quad (2M/\pi)^{1/2}\alpha_{j_n}\left(\frac{X}{\sqrt{M}},E\right)\sin\left[\theta_{j_n}\left(\frac{X}{\sqrt{M}},E\right)\right] \ , \tag{6.31}$$

$$\tilde{G}_{j_n}(X) = -(2M/\pi)^{1/2}\alpha_{j_n}\left(\frac{X}{\sqrt{M}},E\right)\cos\left[\theta_{j_n}\left(\frac{X}{\sqrt{M}},E\right)\right] \ . \tag{6.32}$$

Since our adiabatic curves arrive very close to their asymptotic limits at a reasonable distance (let us denote it R_1), we can define

$$\Theta_{j_n}(E) = \int_{R_0}^{R_1} \alpha_{j_n}^{-2}(R',E)dR' \ , \tag{6.33}$$

which is the additional phase shift that $\tilde{F}_{j_n}(X), \tilde{G}_{j_n}(X)$ accumulate before becoming essentially Bessel functions. With these new quantities the matrix definitions (3.29), (3.30) required for channel elimination are altered to the form

$$\Gamma_{j\gamma} = \begin{cases} U_{j\gamma}\sin(\beta_j + \pi\tau_\gamma) \ , & j \in Q_{\rm e} \\ U_{j\gamma}\sin(\Theta_j + \pi\tau_\gamma) \ , & j \in Q_{\rm n} \\ & \\ U_{j\gamma}\sin\pi\tau_\gamma \ , & j \in P_{\rm e} \\ U_{j\gamma}\sin\pi\tau_\gamma \ , & j \in P_{\rm n} \end{cases} \ , \tag{6.34}$$

$$\Lambda_{j\gamma} = \begin{cases} 0 \ , & j \in Q_{\rm e} \\ 0 \ , & j \in Q_{\rm n} \\ & \\ U_{j\gamma}\cos\pi\tau_\gamma \ , & j \in P_{\rm e} \\ U_{j\gamma}\cos\pi\tau_\gamma \ , & j \in P_{\rm n} \end{cases} \ . \tag{6.35}$$

In the case that our shrunk R_0 value can still accommodate some of the adiabatic curves (meaning they are effectively constant outside of it), we can use the original Bessel functions for their corresponding channels, and $\Gamma_{j\gamma}$, $\Lambda_{j\gamma}$ will use their old definitions (3.29), (3.30) for those channels. The remaining path to DR cross sections is the same as in chapter 3.

6.2.3 Preliminary results

The initial target channels for the DR process in the singlet gerade symmetry, described in the body frame, contain only $l = 0$ and $l = 2$ partial waves. It is because at these energies the $l = 1$ repulsive nuclear states leave the electronic wave functions in the closed-channels regime (see Fig. 6.7). Fig. 6.8 shows our first preliminary results for DR cross sections of $H_2^+ + e^-$ in the gerade symmetry

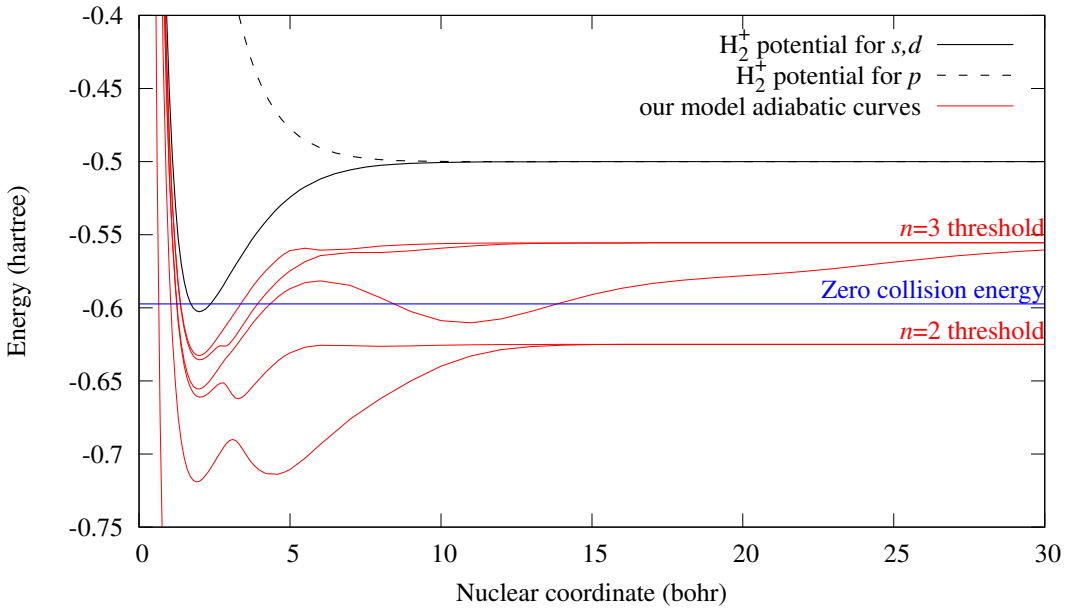

Figure 6.7: The position of the electronic zero collision energy (blue) compared to the nuclear potential curves (black) and adiabatic potential curves (red) with denoted threshold numbers.

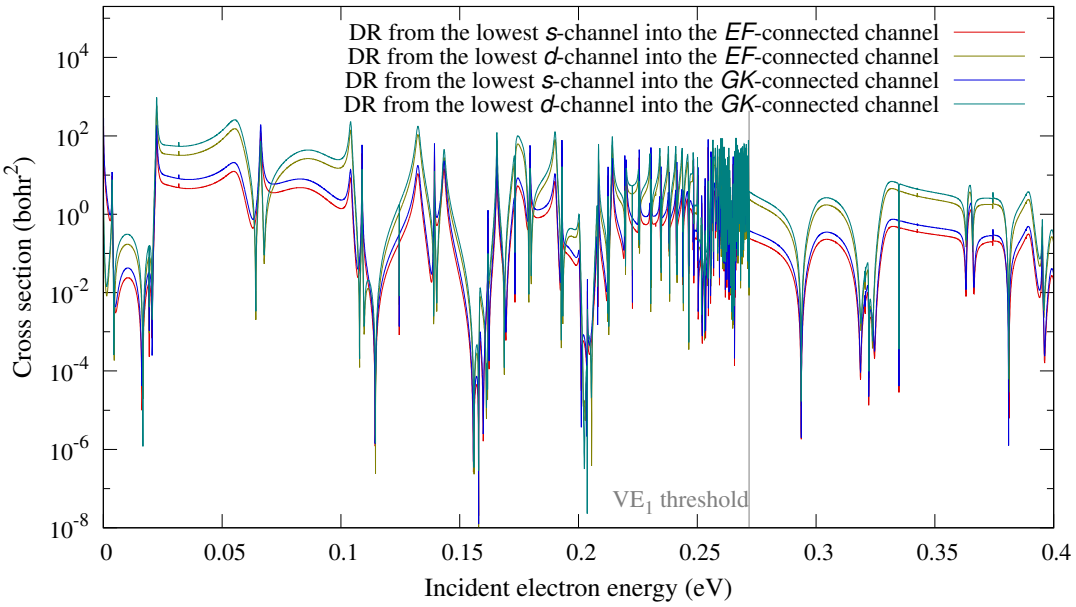

Figure 6.8: DR cross sections computed with our gerade model potential with the expanded two-dimensional R-matrix method. The four curves show the combinations of two incoming and two outgoing channels.

computed with the outlined two-dimensional R-matrix method with box sizes $r_0 = 50$ bohr, $R_0 = 12$ bohr, $R_1 = 50$ bohr. The "Milne treatment" was most necessary for the channels connected to the EF, GK and $H\bar{H}$ curves. As we had hoped, the cross section connected to the lowest channel, which is badly represented by our model, is many orders of magnitude below the others (not shown in the image).

Conclusions

The main focus of this thesis is the development of a theoretical toolkit for a qualitative, as well as quantitative understanding of the two basic processes that drive the dissociative recombination of small molecular cations.

The first of these processes, the indirect mechanism, is always present in DR and it forms a dominant part of the thesis. The theoretical toolkit presented here consists of the multichannel quantum defect theory (MQDT) in combination with the vibrational frame transformation (FT) into the non-hermitian nuclear basis of Siegert pseudo-states. The majority of this toolkit was not developed here but its foundations were created in the pioneering works of Hamilton and Greene [12], Kokoouline and Greene [13]. However, some of the theoretical steps used in these methods were intuitive and there was not a clear theoretical nor numerical evidence that the theory is correct. A comparison with experimental data was not always conclusive as the experiments were not able to reproduce most of the fine structures predicted by the theory due to the finite temperatures and resolutions in the experimental measurements.

Therefore, in order to benchmark and judge this theoretical toolkit, we have developed a "toy model" in the form of a minimal 2D model, in which one coordinate represents the electronic degrees of freedom and the second coordinate describes the nuclear motion. We proposed two methods to solve the model exactly (up to a numerical precision), without making any physically motivated approximations (such as the Born-Oppenheimer approximation). The first method employed the exterior complex scaling (ECS) of both coordinates and its implementation was the subject of my master's thesis. The second method is based on the 2D R-matrix method and it solves the 2D Hamiltonian in a small 2D box. The inelastic cross sections are obtained by a matching of the solutions to the analytic asymptotic functions.

In the first part of the thesis the 2D model is tailored to the indirect DR process of H_2^+ cations in the singlet ungerade symmetry. The comparison of the exact DR cross sections with the results of the above-mentioned toolkit revealed two weak points of our theory:

1. The positions and shapes of the closed-channel resonances were not accurately reproduced due to an approximation in the theory that omits the energy dependence of quantum defects.

2. The presence of collision energy windows (typically just under thresholds of the outgoing electronic states) in which it was impossible to obtain results converged with respect to the size of the nuclear basis of Siegert pseudo-states.

Therefore, this benchmark of our theoretical toolkit resulted in the two following improvements:

1. The implementation of the energy-dependent frame transformation theory for the DR process. Unfortunately, the strict and accurate implementation of the theory of Gao and Greene [6] has led to a deterioration of the results when they were compared with the energy independent FT theory. We have

identified the origin of this setback in the failure of the Born-Oppenheimer approximation (BOA) even in small electronic boxes of 7-8 bohrs. The energy independent FT, as used and implemented in the previous studies, contained a silent correction to the BOA. However, we have found that if the electronic wave function is interaction-free backpropagated to a shorter electronic radius (e.g. 2 bohrs) the DR results are markedly improved and the agreement with the exact results is within 0.1%. The simplified version of the backpropagation procedure was then used in a practical application of this modified toolkit: the DR of HeH^+ cations. The demand for the accurate DR data of HeH^+ has strongly increased after the first astrophysical observation of this presumably oldest molecule of the Universe (Güsten *et al.* [35]). The resulting initial-state resolved DR cross sections computed with the energy-dependent FT were in a very good agreement with the pioneering experimental data from the Cryogenic Storage Ring (CSR) at MPIK in Heidelberg (Novotný *et al.* [36]).

2. We identified that the problematic energy windows in the computed DR cross sections are related to an *ad hoc* procedure in which the nuclear basis was chosen from a doubly complete set of Siegert pseudo-states. It was found that splitting this doubly complete set of states into two independent complete sets is a very problematic procedure. The subset of the bound and outgoing-wave states appeared to be slightly overcomplete and this, albeit very small, error in the completeness was responsible for inaccurate results in the examined energy windows. In order to improve this step, we have implemented the complex nuclear basis from the exterior complex scaling method. The completeness of the resulting nuclear basis is much more accurate, however, the price for this accuracy is paid by the size of the basis – it needs to be about two to three times larger than the basis of the Siegert pseudo-states. The application of our theoretical toolkit to the DR of HeH^+ cations, mentioned above, already employs the nuclear basis of ECS states.

In the second and smaller part of the thesis a possible application of the toolkit to the direct mechanism of DR is explored. Following the indirect study, a new "toy model" of the direct mechanism is proposed in the form of a coupled set of three 2D models. This model is tailored to describe the DR process of the $H_2^+ + e^-$ via singlet gerade channels. The three 2D models represent the three dominant partial waves $l = 0, 1, 2$ that govern, at low collision energies, the electronic degrees of freedom, as well as the dissociation Rydberg channels. The physical nature of the model was tested on the reproduction of some of the known properties of the H_2 molecule, namely

- the positions of the vibronic states,
- the adiabatic curves of the $2p\sigma^2$ closed-channel resonance,
- the adiabatic quantum defects.

These tests have shown that while the model is not quantitatively accurate, it contains all the physical properties reasonably close to the real molecular system.

The implementation of the model was finished and the stability of the computed DR cross sections, with respect to various numerical parameters, was tested during my Ph.D. studies. The resulting cross sections will serve as a benchmark for an approximate theoretical toolkit that is being currently developed in the group.

Bibliography

[1] A. E. Orel and M. Larsson. *Dissociative recombination of molecular ions*. Cambridge University Press, New York, 2008. ISBN 978-0-521-82819-2.

[2] R. von Hahn, A. Becker, F. Berg, K. Blaum, C. Breitenfeldt, H. Fadil, F. Fellenberger, M. Froese, S. George, J. Göck, M. Grieser, F. Grussie, E. A. Guerin, O. Heber, P. Herwig, J. Karthein, C. Krantz, H. Kreckel, M. Lange, F. Laux, S. Lohmann, S. Menk, C. Meyer, P. M. Mishra, O. Novotný, A. P. O'Connor, D. A. Orlov, M. L. Rappaport, R. Repnow, S. Saurabh, S. Schippers, C. D. Schröter, D. Schwalm, L. Schweikhard, T. Sieber, A. Shornikov, K. Spruck, S. Sunil Kumar, J. Ullrich, X. Urbain, S. Vogel, P. Wilhelm, A. Wolf, and D. Zajfman. The cryogenic storage ring CSR. *Review of Scientific Instruments*, 87(6):063115, 2016.

[3] D. Hvizdoš. Two-dimensional model of dissociative recombination. Master's thesis, Charles University in Prague, 2016.

[4] E. S. Chang and U. Fano. Theory of electron-molecule collisions by frame transformations. *Physical Review A*, 6(1):173–185, 1972.

[5] M. J. Seaton. Quantum defect theory. *Reports on Progress in Physics*, 46(2):167–257, 1983.

[6] H. Gao and C. H. Greene. Energy-dependent vibrational frame transformation for electron-molecule scattering with simplified models. *The Journal of Chemical Physics*, 91(7):3988–3998, 1989.

[7] H. Gao and C. H. Greene. Alternative vibrational frame transformation for electron-molecule scattering. *Physical Review A*, 42(11):6946–6949, 1990.

[8] M. LeDourneuf, B. I. Schneider, and P. G. Burke. Theory of vibrational excitation and dissociative attachment: an R-matrix approach. *Journal of Physics B: Atomic and Molecular Physics*, 12(12):L365–L369, 1979.

[9] H. Bachau, E. Cormier, P. Decleva, J. E. Hansen, and F. Martín. Applications of B-splines in atomic and molecular physics. *Reports on Progress in Physics*, 64(12):1815–1943, 2001.

[10] E. L. Hamilton. *Photoionization, Photodissociation, and Long-Range Bond Formation in Molecular Rydberg States*. PhD thesis, University of Colorado, 2003.

[11] Karel Houfek, T. N. Rescigno, and C. W. McCurdy. Numerically solvable model for resonant collisions of electrons with diatomic molecules. *Physical Review A*, 73:032721, 2006.

[12] E. L. Hamilton and C. H. Greene. Competition among molecular fragmentation channels described with siegert channel pseudostates. *Physical Review Letters*, 89:263003, 2002.

[13] V. Kokoouline and C. H. Greene. Unified theoretical treatment of dissociative recombination of D_{3h} triatomic ions: Application to H_3^+ and D_3^+. *Physical Review A*, 68:012703, 2003.

[14] R. Čurík and C. H. Greene. Indirect dissociative recombination of LiH^+ molecules fueled by complex resonance manifolds. *Physical Review Letters*, 98:173201, 2007.

[15] R. Čurík and C. H. Greene. Vibrational excitation and dissociative recombination of the LiH^+ ion. *Molecular Physics*, 105(11-12):1565–1574, 2007.

[16] D. J. Haxton and C. H. Greene. Estimates of rates for dissociative recombination of $NO_2^+ + e^-$ via various mechanisms. *Physical Review A*, 86(6):062712, 2012.

[17] R. Čurík and F. A. Gianturco. Indirect dissociative recombination of $LiHe^+$ ions driven by vibrational Feshbach resonances. *Physical Review A*, 87(1):012705, 2013.

[18] D. J. Haxton and C. H. Greene. Indirect dissociative recombination of $LiH_2^+ + e^-$. *Physical Review A*, 78:052704, 2008.

[19] D. J. Haxton and C. H. Greene. Ab initio frame-transformation calculations of direct and indirect dissociative recombination rates of $HeH^+ + e^-$. *Physical Review A*, 79:022701, 2009.

[20] R. Čurík and C. H. Greene. Inelastic low-energy collisions of electrons with HeH^+: Rovibrational excitation and dissociative recombination. *The Journal of Chemical Physics*, 147(5):054307, 2017.

[21] O. I. Tolstikhin, V. N. Ostrovsky, and H. Nakamura. Siegert Pseudo-States as a Universal Tool: Resonances, S Matrix, Green Function. *Physical Review Letters*, 79:2026–2029, 1997.

[22] O. I. Tolstikhin, V. N. Ostrovsky, and H. Nakamura. Siegert pseudostate formulation of scattering theory: One-channel case. *Physical Review A*, 58:2077–2096, Sep 1998.

[23] M. J. Seaton. Coulomb functions for attractive and repulsive potentials and for positive and negative energies. *Computer Physics Communications*, 146(2):225 – 249, 2002.

[24] M. Aymar, C. H. Greene, and E. Luc-Koenig. Multichannel rydberg spectroscopy of complex atoms. *Reviews of Modern Physics*, 68:1015–1123, 1996.

[25] R. Szmytkowski. Erratum: Variational R-matrix methods for many-electron systems: Unified nonrelativistic theory [Phys. Rev. A 61, 022725 (2000)]. *Physical Review A*, 66:029901, 2002.

[26] E. P. Wigner and L. Eisenbud. Higher angular momenta and long range interaction in resonance reactions. *Physical Review*, 72:29–41, 1947.

[27] K. T. Lu. Spectroscopy and Collision Theory - Xe absorption spectrum. *Physical Review A*, 4:579, 1971.

[28] C. H. Greene and C. Jungen. Molecular applications of quantum defect theory. volume 21 of *Advances in Atomic and Molecular Physics*, pages 51–121. Academic Press, 1985.

[29] C. Jungen and S. C. Ross. Unified quantum-defect-theory treatment of molecular ionization and dissociation. *Physical Review A*, 55:R2503–R2506, 1997.

[30] K.L. Baluja, P.G. Burke, and L.A. Morgan. R-matrix propagation program for solving coupled second-order differential equations. *Computer Physics Communications*, 27(3):299 – 307, 1982.

[31] N. S. Scott, M. P. Scott, P. G. Burke, T. Stitt, V. Faro-Maza, C. Denis, and A. Maniopoulou. 2DRMP: a suite of two-dimensional R-matrix propagation codes. *Computer Physics Communications*, 180(12):2424 – 2449, 2009.

[32] C. W. McCurdy and F. Martín. Implementation of exterior complex scaling in B-splines to solve atomic and molecular collision problems. *Journal of Physics B: Atomic, Molecular and Optical Physics*, 37(4):917–936, 2004.

[33] C. M. Lee. Spectroscopy and collision theory. III. atomic eigenchannel calculation by a Hartree-Fock-Roothaan method. *Physical Review A*, 10:584–600, 1974.

[34] F. Robicheaux. Driving nuclei with resonant electrons: Ab initio study of $(e+H_2)$ $^2\Sigma_u^+$. *Physical Review A*, 43:5946–5955, 1991.

[35] R. Güsten, H. Wiesemeyer, D. Neufeld, K. M. Menten, U. U. Graf, K. Jacobs, B. Klein, O. Ricken, C. Risacher, and J. Stutzki. Astrophysical detection of the helium hydride ion HeH^+. *Nature*, 568(7752):357–359, 2019.

[36] O. Novotný, P. Wilhelm, D. Paul, Á. Kálosi, S. Saurabh, A. Becker, K. Blaum, S. George, J. Göck, M. Grieser, F. Grussie, R. von Hahn, C. Krantz, H. Kreckel, C. Meyer, P. M. Mishra, D. Muell, F. Nuesslein, D. A. Orlov, M. Rimmler, V. C. Schmidt, A. Shornikov, A. S. Terekhov, S. Vogel, D. Zajfman, and A. Wolf. Quantum-state–selective electron recombination studies suggest enhanced abundance of primordial HeH^+. *Science*, 365(6454):676–679, 2019.

[37] J. A. Coxon and P. G. Hajigeorgiou. Experimental Born-Oppenheimer Potential for the $X^1\Sigma^+$Ground State of HeH^+: Comparison with the *Ab Initio* Potential. *Journal of Molecular Spectroscopy*, 193(2):306 – 318, 1999.

[38] L. A. Morgan, C. J. Gillan, J. Tennyson, and Xiushan Chen. R-matrix calculations for polyatomic molecules: electron scattering by N_2O. *Journal of Physics B: Atomic, Molecular and Optical Physics*, 30(18):4087–4096, 1997.

[39] I. Ema, J. M. García de la Vega, G. Ramírez, R. López, J. Fernández Rico, H. Meissner, and J. Paldus. Polarized basis sets of Slater-type orbitals: H to Ne atoms. *Journal of Computational Chemistry*, 24(7):859–868, 2003.

[40] V. Kokoouline and C. H. Greene. Theoretical study of dissociative recombination of C_{2v} triatomic ions: Application to H_2D^+ and D_2H^+. *Physical Review A*, 72:022712, 2005.

[41] O. Novotný, A. Becker, H. Buhr, C. Domesle, W. Geppert, M. Grieser, C. Krantz, H. Kreckel, R. Repnow, D. Schwalm, K. Spruck, J. Stützel, B. Yang, A. Wolf, and D. W. Savin. DISSOCIATIVE RECOMBINATION MEASUREMENTS OF HCl^+ USING AN ION STORAGE RING. *The Astrophysical Journal*, 777(1):54, 2013.

[42] M. M. Madsen and J. M. Peek. Eigenparameters for the lowest twenty electronic states of the hydrogen molecule ion. *Atomic Data*, 2:171, 1971.

[43] L. Wolniewicz and K. Dressler. Adiabatic potential curves and nonadiabatic coupling functions for the first five excited $^1\Sigma_g^+$ states of the hydrogen molecule. *The Journal of Chemical Physics*, 100(1):444–451, 1994.

[44] L. Wolniewicz and K. Dressler. The EF, GK, and $H\bar{H}$ $^1\Sigma_g^+$ states of hydrogen. improved ab initio calculation of vibrational states in the adiabatic approximation. *The Journal of Chemical Physics*, 82(7):3292–3299, 1985.

[45] S. C. Ross and C. Jungen. Multichannel quantum-defect theory of double-minimum $^1\Sigma_g^+$ states in H_2. II. vibronic-energy levels. *Physical Review A*, 49(6):4364–4377, 1994.

[46] C. H. Greene and B. Yoo. Doubly-excited states in the spectrum of molecular hydrogen. *The Journal of Physical Chemistry*, 99(6):1711–1718, 1995.

[47] S. C. Ross and C. Jungen. Multichannel quantum-defect theory of double-minimum $^1\Sigma_g^+$ states in H_2. I. potential-energy curves. *Physical Review A*, 49(6):4353–4363, 1994.

[48] C. H. Greene, A. R. P. Rau, and U. Fano. General form of the quantum-defect theory. II. *Physical Review A*, 26:2441–2459, 1982.

List of Figures

List of Tables

List of Abbreviations

BOA	- Born-Oppenheimer approximation
CSR	- Cryogenic Storage Ring
DR	- dissociative recombination
DVR	- discrete variable representation
ECS	- exterior complex scaling
FEM	- finite element method
FT	- frame transformation
MQDT	- multichannel quantum defect theory
VE	- vibrational excitation

List of publications

[A] Dávid Hvizdoš, Martin Váňa, Karel Houfek, Chris H. Greene, Thomas N. Rescigno, C. William McCurdy, and Roman Čurík. Dissociative recombination by frame transformation to Siegert pseudostates: A comparison with a numerically solvable model. *Phys. Rev. A*, 97:022704, 2018

[B] Roman Čurík, Dávid Hvizdoš and Chris H. Greene. Validity of the Born-Oppenheimer approximation in the indirect-dissociative-recombination process. *Phys. Rev. A*, 98:062706, 2018

[C] Dávid Hvizdoš, Roman Čurík and Chris H. Greene. Backpropagated frame transformation theory: A reformulation. *Phys. Rev. A*, 101:012709, 2020

[D] Roman Čurík, Dávid Hvizdoš and Chris H. Greene. Dissociative recombination of cold HeH^+ ions, *Phys. Rev. Lett.*, 124:043401, 2020